AD-A039 216 TEXAS UNIV AT AUSTIN DEPT OF AEROSPACE ENGINEERING AN--ETC F/G 20/4
WIND TUNNEL EXPERIMENTS ON AN ACTIVELY CONTROLLED, VARIABLE GEO--ETC(U)
MAR 77 J LONG, R STEARMAN F44620-76-C-0072

UNCLASSIFIED AFOSR-TR-77-0638 NL

1 OF 2
AD A039216

AFOSR FINAL Report
Volume II

WIND TUNNEL EXPERIMENTS ON AN ACTIVELY CONTROLLED, VARIABLE GEOMETRY FLUTTER MODEL

by

Jeff Long

and

Ronald Stearman

AFOSR FINAL REPORT

This research was sponsored by the

AIR FORCE OFFICE OF SCIENTIFIC RESEARCH

Office of Aerospace Research

through Contract F44620-76-C-0072

MARCH 1977

AIR FORCE OFFICE OF SCIENTIFIC RESEARCH (AFSC)
NOTICE OF TRANSMITTAL TO DDC
This technical report has been reviewed and is approved for public release IAW AFR 190-12 (7b).
Distribution is unlimited.
A. D. BLOSE
Technical Information Officer

AFOSR Scientific Report
Volume II

Air Force Office of Scientific Research

Contract F44620-76-C-0072

WIND TUNNEL EXPERIMENTS ON AN ACTIVELY CONTROLLED, VARIABLE GEOMETRY FLUTTER MODEL

by

Jeff Long

and

Ronald Stearman

Department of Aerospace Engineering and Engineering Mechanics

The University of Texas at Austin

Austin, Texas 78712

March 1977

ABSTRACT

A reduction in flutter margin can occur for variable geometry aircraft when the wing of the aircraft is swept into the vicinity of the tail. Experiments on an aeroelastic wind tunnel model with active aerodynamic controls demonstrated that the flutter margins of these configurations can be increased through techniques other than the standard structural modifications. Improved margins were attained by employing rapidly responding aerodynamic controls activated by an "optimal" feedback.

ACKNOWLEDGMENTS

The authors wish to acknowledge the support and assistance of the staff of the Aerospace Structura_ Dynamics and Aeroelasticity Laboratory of The University of Texas at Austin during the development of this research program. They also express their appreciation to the Computation Center of The University of Texas for the extended use of their facilities.

Finally, the authors wish to extend their thanks to William Walker, Aeromechanics Division, Air Force Office of Scientific Research, Office of Aerospace Research, for his continued financial support of this program.

Austin, Texas
March 1977

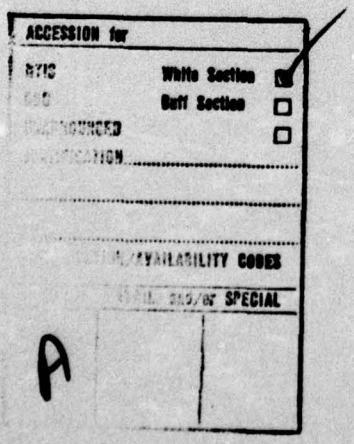

Table of Contents

1. Introduction

This report is a continuation of the investigation of active control technology at The University of Texas at Austin. The goal of the research is to demonstrate that the dynamic stability of an aircraft can be augmented through the use of an active flutter suppression system employing feedback control laws. More specifically the research demonstrates that in the case of a variable geometry aircraft on which the wing sweeps into close proximity with the tail, such as the F-111 or the F-14, the flutter speed of the aircraft can be raised through the use of an active control commanding the movement of control surfaces.

A successful active control might take the place of increased stiffness which must be bought at the expense of more weight. Further, in the case of ejectable stores in which the mass characteristics of the wing change suddenly, through the use of electronic devices the feedback laws can be changed to match each configuration.

The principle was demonstrated experimentally by Griffin[1] on a small model with three degrees of freedom, then Cwach[2] and Pinnamaneni[3] developed and theoretically analyzed control laws. During his dissertation work Cwach developed a computer program which finds an optimal control law. During 1975 and 1976 a half span wind tunnel model was built at The University of Texas. The model was built to the plans of the AFFDL variable-geometry wing tail flutter model[4] with a few minor

variations. A low cost analog computer was designed and built by Bolding[5] through which the control law is implemented.

The entire project has existed through the support of the Air Force Office of Scientific Research and the assistance of the Air Force Flight Dynamics Laboratory.

This report describes the wind tunnel tests conducted at The University of Wichita 7' x 10' low speed wind tunnel. The results are presented which include passive flutter speeds and flutter speeds with a control law implemented. The physical meaning of the control law is described, i.e., it is explained how the control law breaks the aerodynamic coupling between the wing and tail. Finally, corrections are made to the structural dynamic model previously defined by Lehman[6] and the analytic predictions of passive flutter. The subsequent flutter margin gained through the use of active control is discussed.

2. Analytical Flutter Studies

2.1 Review of Theory

The equations of motion which define the response of a flexible aircraft to an external force are developed in Reference 2 by Cwach. That development is presented briefly in Appendix A. Some of the results are presented in this discussion.

The equation of motion can be expressed as:

$$\sum_{s=1}^{n} \left[m_{rs} - \frac{(1+ig)}{\omega^2} K_{rs} + 1/2 \frac{\rho b^2}{2} Q_{rs} \right] q_s(\omega)$$

$$= - \sum_{j=1}^{m} \left[m_{\delta_{rj}} + 1/2 \frac{\rho b^2}{k^2} Q_{\delta_{rj}} \right] \delta_j(\omega) - 1/2 \frac{b^2 \rho}{k^2} Q_{F_r} W_g(\omega) \qquad (2.1)$$

$$(r = 1,2,\ldots n)$$

where

Q_{rs} = generalized force with deflection in r^{th} mode and pressure in s^{th} mode

n = no. of generalized coordinates

m = no. of controls

$m_{\delta_{rj}}$ = generalized mass of control surface (see Appendix A)

$Q_{\delta_{rj}}$ = generalized force for control surface (see Appendix A)

k = $\omega b/V$ = reduced frequency

m_{rs} = generalized mass of the structure (see Appendix A)

K_{rs} = generalized stiffness of the structure (see Appendix A)

$\delta_j(\omega)$ = deflection (radians) of j^{th} control surface

$W_g(\omega)$ = aerodynamic flow disturbance such as wind gust

Q_{F_r} = generalized force associated with wind gust (see Appendix A)

b = reference length

In matrix form the equation becomes:

$$\left[[m] - \frac{1 + ig}{\omega^2}[K] + [Q]\right]\{q\} = -[Q_c]\{\delta\} - \{Q_F\} W_G \qquad (2.2)$$

In (2.2) the constant $1/2\ \frac{\rho b^2}{k^2}$ has been absorbed into the aerodynamic force terms and the $m_{\delta_{rj}}$ terms have been included in the $[Q_c]$ matrix.

2.2 Passive Flutter

The $\{\delta\}$ terms are the control feedback mechanism. The deflection of the control surface (δ) is prescribed by the control law and is a function of the generalized coordinates (q). The passive (uncontrolled) response of the flexible aircraft is obtained by setting the control law (hence δ) and the aerodynamic disturbance equal to zero. The resulting complex eigenvalue equation is

$$[K]^{-1}\left[[m] + [Q]\right]\{q\}_j = \lambda_j \{q\}_j \qquad (2.3)$$

The solution of (2.3) gives n eigenvalues and eigenvectors where $\lambda_j = (1 + ig_j)/\omega_j^2$ are the eigenvalues and $\{q_j\}$ the eigenvectors. Each eigenvalue and eigenvector represents a possible mode of harmonic motion with frequency ω_j (the eigenvalue). The eigenvector is complex and represents the relative magnitude and phase of each generalized coordinate in the j^{th} mode of vibration. The g_j represent the amount of structural damping necessary to maintain harmonic motion in the j^{th} mode. When g_j is the same as the actual structural damping harmonic motion takes place. When g_j is less the motion is damped out. The flutter predictions are usually conservative if the available structural damping is unknown and hence assumed to be zero.

The generalized aerodynamic force terms are a function of reduced frequency ($k = \frac{\omega b}{v}$) and hence reduced frequency must be specified in order to calculate them. The method used in this study to predict flutter has been to:

1) Compute the aerodynamic force terms for a range of reduced frequencies
2) Solve the eigenvalue problem to obtain ω_j , q_j , g_j
3) Plot both ω_j and g_j vs. air speed
4) Flutter speed is that speed at which the damping crosses the zero line (or the actual structural damping line if known) in the positive direction.

2.3 Controlled Flutter

Again following arguments presented by Griffin[1] a method of flutter suppression may be demonstrated. The feedback control law is assumed to be of the form:

$$\{\delta_f\} = [C_R + iC_I]\{q\} \qquad f = 1,2,\ldots m \tag{2.4}$$

where $[C] = [C_R + iC_I]$ is the complex control law relating angular deflection of the control surface to the complex vector of generalized coordinates. This type of control law is similar to that presented by Nissim[7].

Now substituting (2.4) into (2.2) and rearranging we obtain the equation of motion governing response of the aircraft employing active controls (W_g assumed to be zero):

$$[K]^{-1}\left[[m] + [Q] + [Q_c][C]\right]\{q\}_j = \frac{1 + ig_j}{\omega_j^2}\{q\}_j \tag{2.5}$$

Letting $[Q'] = [Q] + [Q_c][C]$ we can rewrite (2.5) as

$$[K]^{-1}\left[[m] + [Q']\right]\{q\}_j = \frac{1 + ig_j}{\omega_j^2}\{q\}_j \tag{2.6}$$

and employ the same flutter analysis techniques used in the passive flutter case.

2.4 Control Law and Sensor Displacement

The feedback signal originates at sensors placed on the lifting surfaces of the aircraft. Define

$$[z] = [F]\{q\} \tag{2.7}$$

where

- $[z]$ is the complex vector of sensor displacements
- $[F]$ is a matrix of displacements of each sensor due to a unit value of a generalized coordinate. F_{ij} is displacement of i^{th} sensor due to a unit value of the j^{th} generalized coordinate.

In the experiment described in this report two sensors were used: one on the wing near the tip and one on the tail near the tip. This placement was determined by Cwach[2].

Assuming p sensors on the lifting surfaces the feedback control law may take the form:

$$\underset{m\times 1}{\{\delta\}} = \underset{m\times p}{[\bar{C}_R + i\,\bar{C}_I]}\,\underset{p\times 1}{\{z\}} \tag{2.8}$$

where $[\bar{C}] = [\bar{C}_R + i\bar{C}_J]$ relates control deflection to sensor displacement.

Substituting (2.7) into (2.8):

$$\underset{m\times 1}{\{\delta\}} = \underset{m\times p}{[\bar{C}_R + i\bar{C}_I]}\ \underset{p\times n}{[F]}\ \underset{n\times 1}{\{q\}} \tag{2.9}$$

then

$$[C'_R + iC'_I] = [\bar{C}_R + i\bar{C}_I]\,[F] \tag{2.10}$$

and

$$\{\delta\} = [C'_R + iC'_I]\,\{q\} \tag{2.11}$$

which is the same form as (2.4).

2.5 Physical Description of Control Mechanism

The theory behind feedback control has been presented but it is also possible to visualize the problem in a physical way. Imagine viewing a cross section of the wing and tail of a swept wing aircraft as illustrated in Figure 13. If the aircraft is disturbed by a gust the wing will bend up and the angle of attack at the cross section will cause an induced downwash on the tail surface (Fig. 14). This provides lift on the tail surface in the direction of the downwash. At the same time torsional coupling of the wing and tail is providing a restoring force in the same direction. The wing and tail twist back towards and beyond normal position and the same phenomenon occurs in the opposite direction. At the critical airspeed these oscillations diverge causing flutter.

The feedback mechanism senses motion of the wing and tail and commands the tail to pitch in such a manner that the induced downwash

no longer causes lift as shown by the dotted line on Figure 14 representing the altered tail position due to feedback control. This breaks the aerodynamic coupling between wing and tail providing a flutter suppression mechanism.

3. The Model

The U.T. half span wing-tail flutter model was built to the design of a similar AFFDL model[4]. The model and avionics were built under the direction of Bolding[5] and the model description is presented in Appendix B. A structural dynamic model of the wind tunnel model was defined by the members of the Aerospace Structural Dynamics Laboratory, and the theory behind that definition appears in Appendix C. Prior to the actual wind tunnel test changes were made to the model and instrumentation of the model was performed.

3.1 Instrumentation

Instrumentation of the wind tunnel model was accomplished to ensure that the wind tunnel test be well documented and enough information gathered to allow a complete analysis. Strain gauges were applied to both the wing and tail roots to provide bending and torsion information of the spar roots. The wing pitch and roll springs carry strain gauges to provide bending information from those springs. The output from the tail LVDT which is the analog representation of tail pitch was also monitored. The outputs of the accelerometers in the wing and tail were monitored besides their primary function as signal generators for the avionics (control law). The recording devices employed were a Hewlett Packard seven channel tape recorder and a Honeywell seven channel visicorder. Visicorder representations of some of this

information is presented later in this report.

3.2 Changes to Dynamic Model

Before taking the model to the wind tunnel an attempt was made to modify the dynamic characteristics in such a way that the predicted flutter speed would be lowered. Two changes were made: 1) mass was added to sections six and seven of the wing (the bottom two wing sections) and 2) the flexibility of the pitch spring was increased. The new values of the mass characteristics and pitch spring flexibilities are presented in Table 1.

After the hydraulic system for the model was commissioned it was discovered that the tail pitch had significant static flexibility. The flexibility was measured and is also presented in Table 1. The inclusion of tail pitch flexibility necessitated the addition of a structural node. Previously, in the assembly of the model flexibility, structural node 28 (see Figure 15) was constrained (flexibility of zero) so that the deflections would not be unbounded (see Appendix D). The flexibilities of all other nodes were calculated relative to node 28. For the tail to have pitch flexibility about its pitch axis, node 28 must be free to move since it lies on the tail and off the pitch axis. A node was added on the pitch axis above the pitch swivel point. The new structural point was assigned a mass of zero so that it would not disturb the previously defined mass model. Since both node 28 and 29 lie on the tail carry through, assumed to have zero bending flexibility, the flexibility is also undisturbed except for the tail pitch

flexibility which may now be added (see Appendix C). It was suspected that the tail pitch flexibility would raise the flutter speed. An analysis was performed and the results are presented in Table 2. The predicted flutter speed[6] with none of the changes made is 137 ft/sec; with the mass and spring changes the predicted flutter speed is 107 ft/sec; and with tail pitch flexibility added the predicted flutter speed is 116 ft/sec.

4. Experimental Procedure and Results

4.1 Implementation and Measurement of Control Law

When a control law has been selected it must be programmed into the system. That is the function of the analog avionics described in Appendix B.

As previously mentioned, there are two sensors, one in the wing and one in the tail, each with its own programmable channel. For a system with one control surface and two sensors such as the U-T wing stabilator system used in this investigation, the control law is a two element law. Each sensor is associated with one of the elements (see Section 2.4) and vice versa, i.e., there is a one to one correspondence. The elements are complex numbers and therefore carry both gain and phase information. Each channel may be programmed with the appropriate gain and phase (see Fig. 2). In practice this is accomplished by measuring the signal amplitude of the output of integrator B for a given sensor displacement and measuring its phase in relation to an actual harmonic sensor displacement. Over the range of frequencies which the avionics system must handle (zero to twenty c.p.s.) the gain and phase response of the electronic stages is flat. A similar measurement is made between a signal fed to the servoamplifier stage and the output of the stabilator pitch sensor (LVDT). The response of the hydraulic system varies with frequency. The plots of phase and gain

versus frequency are presented in Figures 3 and 4. The intermediate stages are adjustable and may be programmed with the correct gain and phase to accomplish the control law. All the phase shifts must add up to the prescribed control law phase shift and the product of the gains must equal the control law gain.

Conversely, after a control law has been used in the wind tunnel it must be measured (as a check). First, the sensor displacement calibration factor must be determined. Each sensor is displaced a given amount and the signal change at Integrator B output is measured. The output from the second stage of integration (Integrator B) is the analog reprsentation of displacement, i.e., it is the acceleration signal integrated twice. Units for the sensor displacement factor are volts/foot. At this point a signal may be input to the first gain and phase shifting stage and the tail pitch response measured. This gives the tail pitch factor with units radians/volt. The two factors are complex (giving amplitude and phase information) and when multiplied together give $[\bar{C}]$ in equation (2.9), i.e.,

$$\underset{(\text{rad/ft})}{[\bar{C}]} = \underset{(\text{volts/ft})}{\text{SDF}} \cdot \underset{(\text{rads/volt})}{\text{TPF}} \qquad (4.1)$$

The $[F]$ matrix in equation (2.7) is obtained from the mode shapes. Each mode shape used in the analysis must be interpolated to the sensor position. (Remember F_{ij} is displacement of i^{th} sensor in j^{th} mode.) The measured factors as used in the wind tunnel and the $[F]$ matrix are presented in Table 3.

4.2 Experimental Mode Shapes

With the changes to the model described in Section 3.2 it becomes desirable to redefine the mode shapes both analytically and experimentally. With the redefined dynamic model and a numerical eigenvalue solver it was routine to calculate new mode shapes and frequencies (see Appendix D). Before the changes the mode shapes were easily measured. After the changes the fourth, fifth and sixth modes became very difficult to tune and measure, and in fact were not satisfactorily measured using the techniques presently available in the U-T Structural Dynamics Lab. Using the analytical mode shapes and frequencies as a guide it became possible to find the modes even if their measurement was not precise. An example was the fourth mode. Previously the shaker was attached to node 28 (see Fig. 5). After the corrections node 29 was used. Using node 29 no mode shape was found to resemble mode 4. Modes one, two and three were matched closely. Modes five and six were matched only approximately. Moving the shaker to a point close to node 17 on the wing carry-through a very lightly damped mode shape was found resembling approximately the fourth analytic mode shape with good frequency matching. A check of the orthogonality of the experimental mode shapes consisted of a calculation of the generalized masses using the measured lumped mass matrix (see Appendix C) and the experimental mode shapes:

$$[m] = [H]^T [M] [H] \qquad (4.2)$$

where

[m] is the matrix of generalized mass

[H] is the mode shape matrix

[M] is the diagonal lumped mass matrix

If the generalized mass matrix is diagonally dominant the mode shapes are considered (approximately) orthogonal. (If the mode shapes are actually orthogonal with respect to [M] then all off diagonal terms are zero). While the diagonal terms are the largest, the off diagonal are larger than permissible for accurate flutter prediction. The mode shapes, normalized to a vector magnitude of one, are listed in Table 4 and the generalized masses are listed in Table 5. The experimental mode shapes are presented in Figure 6 and the calculated mode shapes are presented in Figure 7.

4.3 Passive Flutter Studies

Before attempting the controlled flutter tests the passive flutter speeds were to be determined. All of the wind tunnel testing was done with a torsion bar length of sixteen inches and a wing-tail separation of .25 ft. The fuselage flexibility was measured and is listed in Table 1.

It was determined that the best method available to our experimental set-up for identifying a flutter speed would be to perturb the model suddenly at successively increasing speeds, beginning with a speed well below our predicted flutter speed. A circuit was

incorporated in the servoamplifier stage (see Fig. 2) which allowed a short pulse of adjustable amplitude to be applied to the tail hydraulic actuator. This would be similar to pulsing an aircraft's control system. The response of the system is displayed in Appendix E by means of visicorder traces. Trace A is tail bending strain information, trace B is wing accelerometer, trace C is tail accelerometer, trace D is wing bending, trace E is tail pitch and trace F, when present, is wing torsion. The gains of each trace are adjusted individually for readability and vary from trace to trace and figure to figure.

The wing bending response was the most valuable in determining the onset of flutter. The wing bending trace was used to estimate system damping. The amplitudes of successive peaks on the trace immediately after pulsing were measured and the estimated damping calculated using the logarithm decrement method. The estimated V-g plots for 60°, 45° and 30° sweep cases are shown in Figures 8, 9 and 10, respectively. This procedure provided the experiment with a good warning of when the model would actually flutter. When flutter did occur with the feedback controls inactive, the tunnel was immediately turned off to prevent model damage.

An alternate flutter excitation method was used at each trial speed. Using an oscillator input to the tail servoamplifier it was possible to give the tail a continuous harmonic motion of adjustable amplitude and frequency. The frequency was swept slowly from one to twenty cycles per second. Several of these response traces are presented in Appendix E, one for 60°, two for 45°, and one for 30°

sweep case. The model fluttered with a tunnel speed about one mile per hour slower using the continuous harmonic excitation than using the pulse method but there was no ready method for estimating damping using the harmonic excitation, therefore both methods were employed. The passive flutter speeds and frequencies as determined by this method are presented in Table 2.

4.4 Controlled Flutter Studies

For the controlled flutter studies only the pulse method was used. Frequency sweeping was not possible because motion of the aerodynamic surfaces excites the feedback system and a forced harmonic tail motion would mask or distort flutter motion. Controlled flutter tests were accomplished for the 60° sweep case. The model was pulsed at test speeds from slightly below the passive flutter which was 116 mph up to 125 mph. The speed was then incremented slowly to 139 mph when uncontrollable flutter occurred causing structural damage. Above 125 mph pulsing was not really necessary as there was sufficient buffeting of the model. Several visicorder traces are presented in Appendix E which were taken during controlled tests. Some of these traces represent pulsed reponses and some show responses to aerodynamic buffeting. The traces taken during speeds of 128 and 130 mph show only aerodynamic buffeting of the wing and the resulting movement of the tail. Note that the motion of the tail pitch matches the motion of wing bending as it should in order to diminish the aerodynamic coupling

as described in Section 2.5. Occasionally the buffeting would be enough to initiate a more violent response similar to the pulsed responses before the controls could damp it out. Notice on the controlled test traces that tail pitch leads wing bending by about 30 degrees as the control law specifies while tail bending is of much smaller amplitude. The feedback control law ($[\bar{C}]$ in Equation (2.9)) is presented graphically in Figure 16.

5. Analytical Procedures and Results

The present study is primarily experimental. Theoretical analysis was employed to aid the experimental investigation but the purpose of the project was the experimental investigation of an active flutter suppression system. Previous studies[1,2,3] associated with this project handled the theoretical investigation of feedback control of flutter. They demonstrated the feasibility, and computer codes were generated which aided the experimental work greatly.

5.1 Mode Shape Calculation

The mode shape calculation was performed so that the generalized mass, stiffness, and aerodynamic force terms could be calculated for the flutter prediction and subsequent control law investigation (see Appendix A). In this case experimental work was done to aid the analysis. It was desired that the calculated mode shapes be very close to the actual mode shapes. To this end a detailed experimental definition of the structural dynamics model was performed (Appendix C) providing a lumped parameter model of the masses and flexibilities of the model. With mass and flexibility determined, mode shapes and frequencies were calculated by applying a numerical eigenvalue solver to the expression:

$$[K]^{-1}\,[M']\,[h_r] = [h_r]\,[\,\omega^2\,] \qquad (5.1)$$

where

$[K]^{-1}$ = inverted stiffness or flexibility matrix

$[M']$ = constrained mass matrix

$[h_r]$ = matrix of relative eigenvectors.

For a system with a free-free rigid body degree of freedom the structural flexibility is not defined until the system is constrained from moving in the rigid body mode[8,9]. This is accomplished analytically by modifying the mass matrix by a constraint matrix as follows (see also Appendix D):

$$[M'] = [C]^T [M] [C] \tag{5.2}$$

where

$[C] = [I] - \frac{1}{I_c} \{x\} \{x\}^T [M]$, the constraint matrix defined in Appendix D for a system with only a roll rigid body degree of freedom

I_c = mass moment of inertia of system about roll axis

$\{x\}$ = vector of mass point displacements due to unit rigid body motion.

Having calculated the relative modes, the absolute or actual modes may be calculated by again using the constraint matrix:

$$[h_A] = [C] [h_r] \tag{5.3}$$

The rigid body mode may then be calculated by the method in Appendix D.

5.2 Flutter Determination

With the mode shapes calculated the aerodynamic stability of the model may be investigated analytically. Aerodynamic influence coefficients are calculated using a doublet-lattice code[10]. Then, using the mode shapes, generalized aerodynamic forces are calculated. The generalized masses are calculated from the lumped mass matrix and the calculated mode shapes as in equation 4.2, and the generalized stiffnesses are calculated by multiplying the generalized mass by the corresponding eigenvalue squared:

$$[k] = [m] [\omega^2] \tag{5.4}$$

Flutter is then analyzed by the method described in Chapter 1.

V-g curves have been plotted from the analytical flutter analysis for both the passive and controlled cases. The plots are presented in Figures 11 and 12. As indicated in the figures the predicted flutter speed is lower than the actual flutter speed of 169 ft/sec. Also the predicted flutter margin using the measured feedback control is only about 7 ft/sec while the flutter margin measured in the wind tunnel was on the order of thirty feet per second. Part of the discrepancies may be attributed to the doublet lattice code, but a large part of it must be attributed to differences between the calculated and actual mode shapes and inaccuracies in control measurement.

There are, however, some characteristics of the actual controlled case which Figure 12 does reveal. With the control law active, the model is dynamically unstable in the second mode at zero

and low airpseeds. The analysis allowed us to predict this and a flow switch was installed on the model which held the controls off until the airspeed reached fifty feet per second. Further, we observed during the wind tunnel test that the model had less damping at speeds below the flutter speed with controls on than with controls off. Figures 11 and 12 predict this also.

The analysis predicts flutter with the third natural vibration mode dominant. From Figures 6 and 7 it can be seen that the analytical and experimental third modes are almost identical. Wing and tail tips are in phase and the wing is subjected to torsion. The visicorder traces reveal that the wing and tail sensors are moving in phase in the flutter mode and the wing torsion signal has a large amplitude verifying third mode flutter.

From Figure 12 it can be seen that damping in the fifth natural vibration mode is positive over much of the test range including speeds below the observed flutter speed. The actual damping of the fifth mode was less than the structural damping because it was not possible to excite a fifth mode flutter over any of the tunnel test speeds. A very small oscillation was observed visually during the tunnel tests which was approximately thirteen cycles per second. The amplitude was so small that the recording of these vibrations was lost in the instrumentation noise.

6. Conclusions

It has been demonstrated, theoretically, and now experimentally, that feedback control is a feasible flutter suppression mechanism. A twenty percent increase (over the uncontrolled configuration) in flutter speed was achieved using feedback control on the U-T Wing-Tail flutter model. While the experiment was a success there are some refinements which could be made.

The experimental natural vibration modes should be defined more precisely. For the analytical flutter predictions the calculated modes were used because the experimental modes were not orthogonal with respect to the lumped mass matrix. The structural dynamic model was defined experimentally and with good accuracy, therefore, the calculated modes seemed the better choice. Better definition of the experimental modes would add confidence to the analysis and may provide a more accurate flutter prediction.

With more accurate modes a new optimal control law could be calculated using the method of Cwach[2] which may provide even more flutter margin. It is not likely that the control law used in the wind tunnel was optimal for the configuration.

There are several changes which could be made to the wind tunnel model which would make it less susceptible to damage when flutter occurs and may actually extend the flutter margin.

Flutter occurred during the controlled tests due to the failure of a structural part which had been fatiguing in flexure during the tests. After examination it was decided that the part was improperly designed. The recommended model changes have been explained to the U-T Structural Dynamics staff and will not be listed here.

Tables

Table 1

Corrections to Dynamic System Model

Defined in Reference 6

Experimental Wing Mass

Section	Mass x 10^2 (slug)	Unbalance x 10^3 (slug-ft)	Inertia (slugs-ft^2 x 10^3)
6	2.400	2.61	1.54
7	2.669	2.09	.950

Pitch Spring Flexibility = 7.5615×10^{-4} rad/in-lb

Tail Pitch Flexibility = 6.5535×10^{-4} rad/in-lb

Fuselage Torsional Flexibility = 4.524×10^{-4} rad/in-lb

Table 2

Flutter Speeds

Torsion Bar Length = 16", Wing Tail Separation = 3"

Sweep	Dynamic Configuration	Calculated V_f (ft/sec)	Experimental V_f (ft/sec)	f_F (cps)
60°	A	137		6.8
60°	B	107		5.7
60°	C	116		5.2
60°	C		169	5.9
45°	C		169	5.9
30°	C		183	5.9
60°	D		204	5.9

A: Unmodified[6]

B: 20° of wing mass added at wing tip and pitch spring flexibility increased by 50%

C: Same as B with tail pitch flexibility added

D: Same as C with feedback controls active

Table 3

Control Law and F Matrix

$$[\bar{C}] = [.2472 + .1315\,i \quad , \quad .0972 - .2991\,i]$$

$$[F] = \begin{bmatrix} .2847 & -.3098 & -.2700 & .2934 & -.1561 & .3609 \\ .2748 & .3787 & -.3730 & .1398 & .4176 & .0990 \end{bmatrix}$$

Table 4

Experimental Mode Shapes

60° Wing Sweep

Torsion Bar Length = 16", Wing Tail Separation = 3"

Structural Point No.	Mode 1	Mode 2	Mode 3	Mode 4	Mode 5	Mode 6
1	.073	.025	.030	-.132	.126	-.088
2	.103	.006	.031	-.134	.093	-.082
3	.131	-.017	.017	-.110	.069	-.057
4	.162	-.066	-.019	-.105	.039	-.037
5	.193	-.102	-.065	-.091	.028	-.024
6	.225	-.176	-.157	-.164	.075	-.051
7	.257	-.233	-.250	-.347	.153	-.109
8	.149	.162	.287	.451	-.141	.071
9	.178	.146	.269	.457	-.186	.101
10	.201	.107	.263	.419	-.213	.133
11	.227	.052	.212	.322	-.239	.156
12	.252	-.102	.134	.177	-.216	.150
13	.278	-.878	.025	.159	-.171	.114
14	.304	-.187	-.124	.056	-.057	.048
15	.792	.077	.124	.134	.039	-.035
16	.104	.148	.169	.000	.275	-.221
17	.042	.032	.050	.000	.072	-.048
18	.078	.165	-.074	.000	.054	.173
19	.119	.206	-.154	.000	-.612	.102
20	.116	.247	-.228	.019	-.078	.031
21	.204	.340	-.306	.047	-.299	-.245
22	.245	.382	-.339	.073	-.404	-.459
23	.149	.176	-.128	.000	.329	.323
24	.178	.203	-.060	.000	.269	.289
25	.210	.233	-.226	.021	.105	.109
26	.242	.335	-.290	.051	-.165	-.214
27	.274	.340	-.325	.079	-.329	-.476
28	.097	.140	-.070	.000	.179	.187

Table 4 (continued)

Calculated Mode Shapes

60° Wing Sweep

Torsion Bar Length = 16", Wing Tail Separation = 3"

Structural Point No.	Mode 1	Mode 2	Mode 3	Mode 4	Mode 5	Mode 6
1	.074	-.008	.033	-.236	.028	.071
2	.103	-.035	.031	-.342	.075	-.012
3	.132	-.065	.022	-.398	.108	-.093
4	.163	-.110	-.020	-.412	.120	-.158
5	.194	-.164	-.087	-.344	.091	-.126
6	.219	-.233	-.209	-.244	.006	.117
7	.258	-.299	-.299	.060	-.123	.417
8	.151	.051	.293	.121	.030	.144
9	.179	.025	.298	.066	.078	-.005
10	.203	-.008	.283	.047	.115	-.186
11	.229	-.055	.238	.064	.131	-.362
12	.253	-.112	.158	.133	.108	-.443
13	.268	-.188	.007	.189	.032	-.285
14	.294	-.263	-.130	.394	-.092	.011
15	.079	.031	.125	-.008	-.101	.149
16	.104	.034	.175	.006	.007	.149
17	.042	.026	.052	-.028	-.036	.150
18	.079	.108	-.105	.043	.140	.098
19	.121	.163	-.152	.056	.177	.117
20	.163	.222	-.212	.081	.254	.142
21	.205	.282	-.277	.108	.334	.147
22	.247	.343	-.347	.139	.429	.149
23	.150	.161	-.019	-.085	-.341	-.222
24	.179	.206	-.079	-.054	-.244	-.190
25	.212	.258	-.148	-.019	-.135	-.160
26	.243	.310	-.227	.028	.021	-.104
27	.276	.364	-.308	.077	.184	-.051
28	.098	.106	-.018	-.049	-.194	-.117

Table 5

Experimental Generalized Masses

$[M_{ij}]$

(slug-ft^2 × 10^3)

10.60	3.49	0.54	3.08	1.02	0.66
	9.46	-0.67	4.63	1.74	0.46
		10.51	-7.14	0.02	0.43
			12.64	-5.87	3.11
	SYMMETRICAL			12.85	0.26
					10.37

Figures

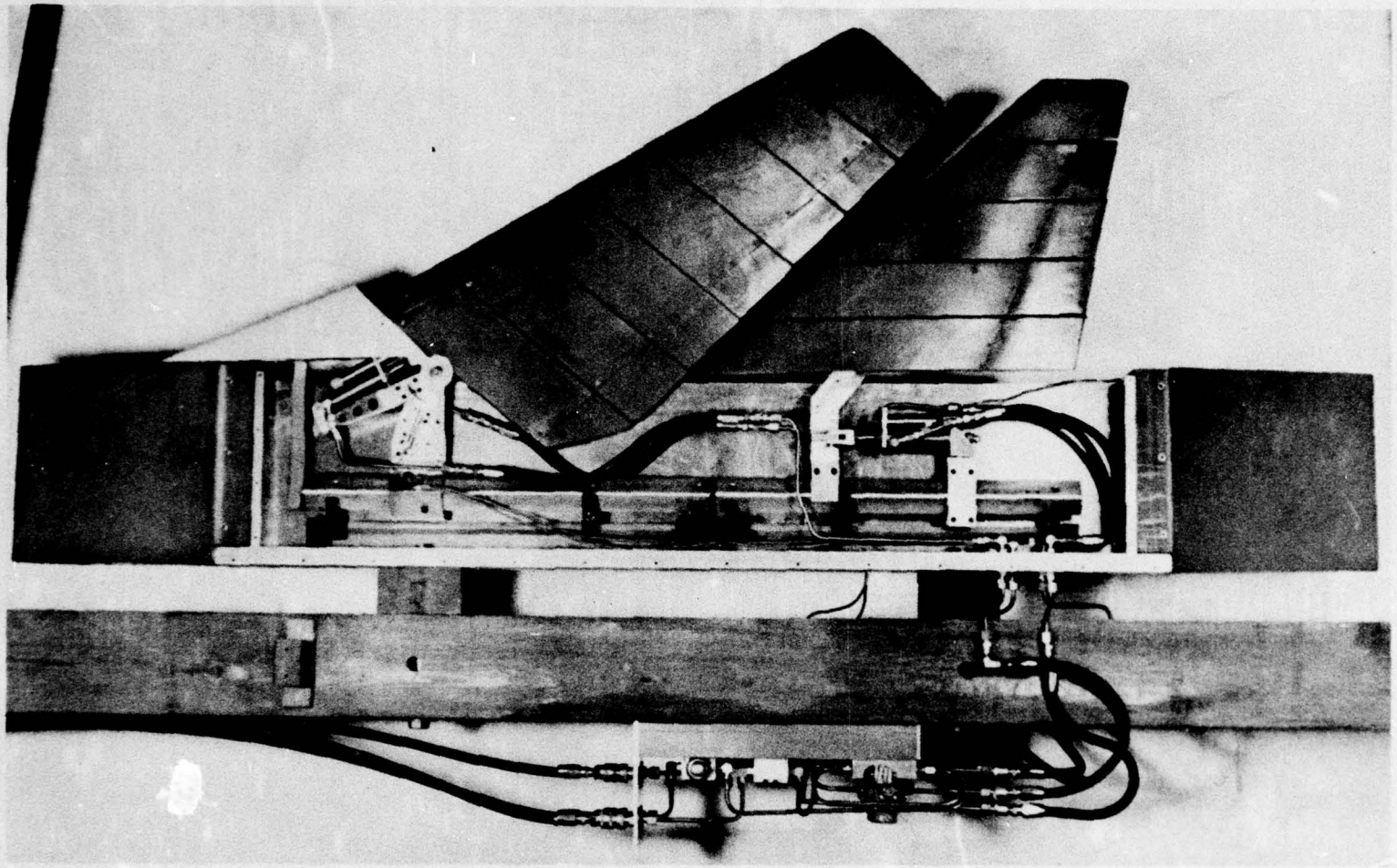

Figure 1. U-T Variable Geometry Wind Tunnel Model for Actively Controlled Flutter Suppression

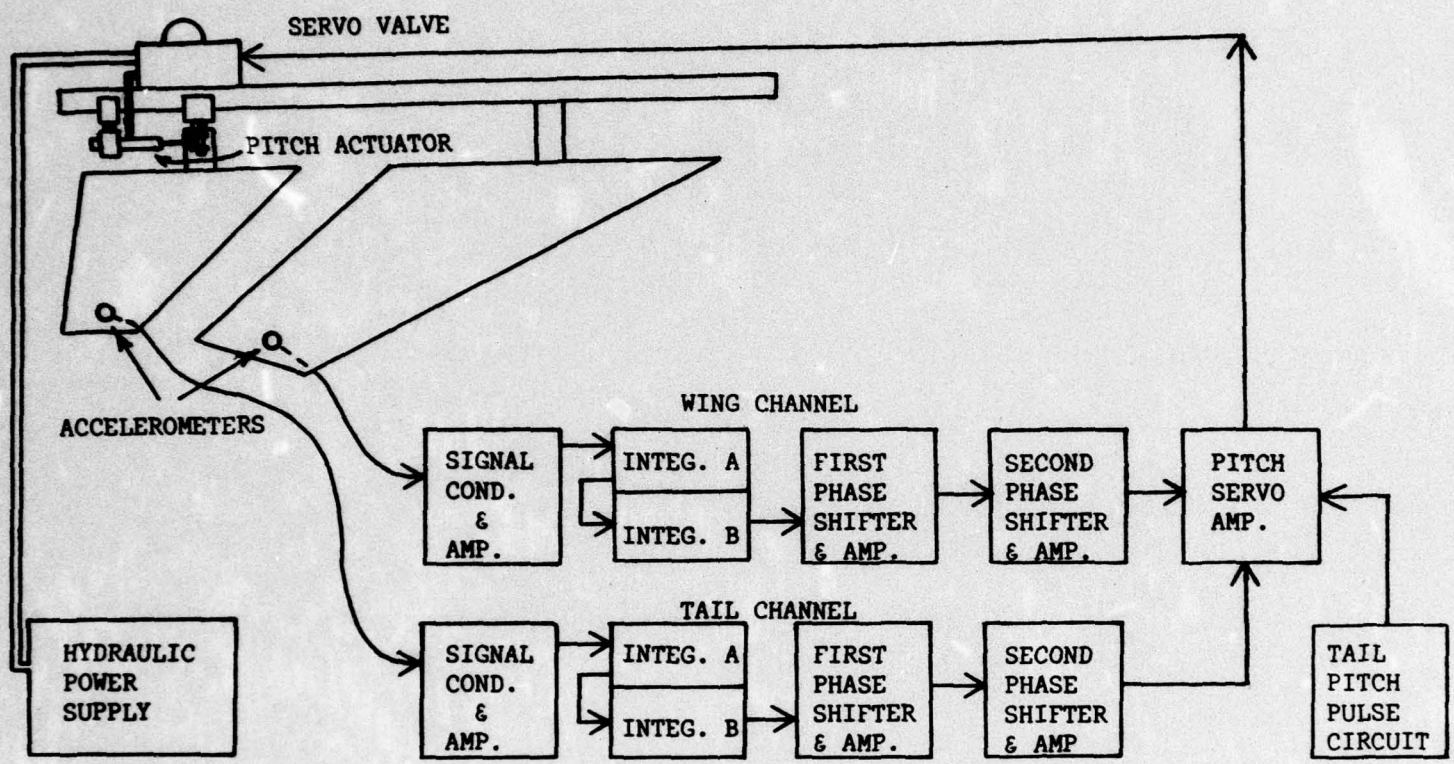

Figure 2. Diagram of Feedback Control System

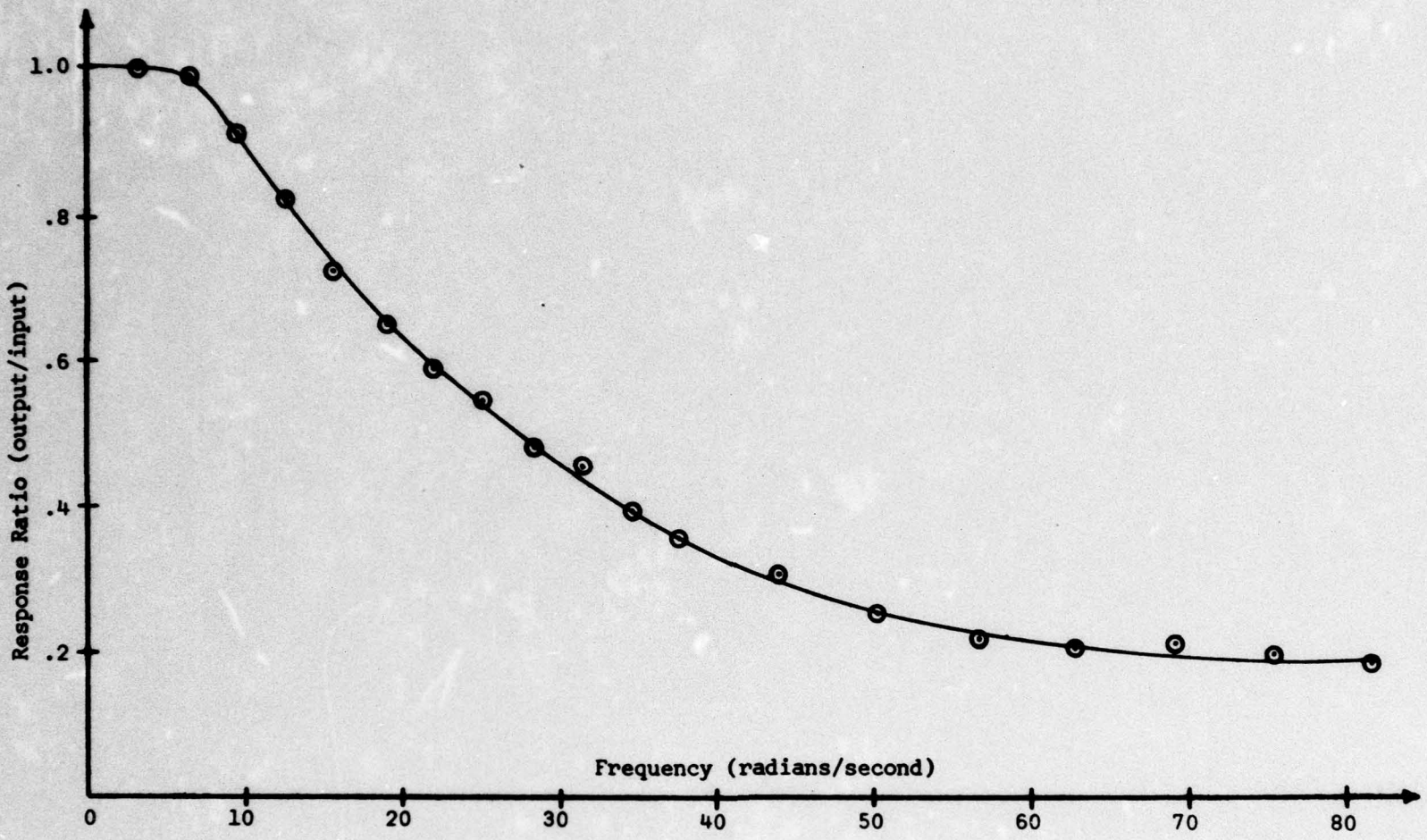

Figure 3. Amplitude Response of Tail Pitch to Servo Amp Signal (Hydraulic System Response). Response Ratio is Normalized to One at Frequency of Zero.

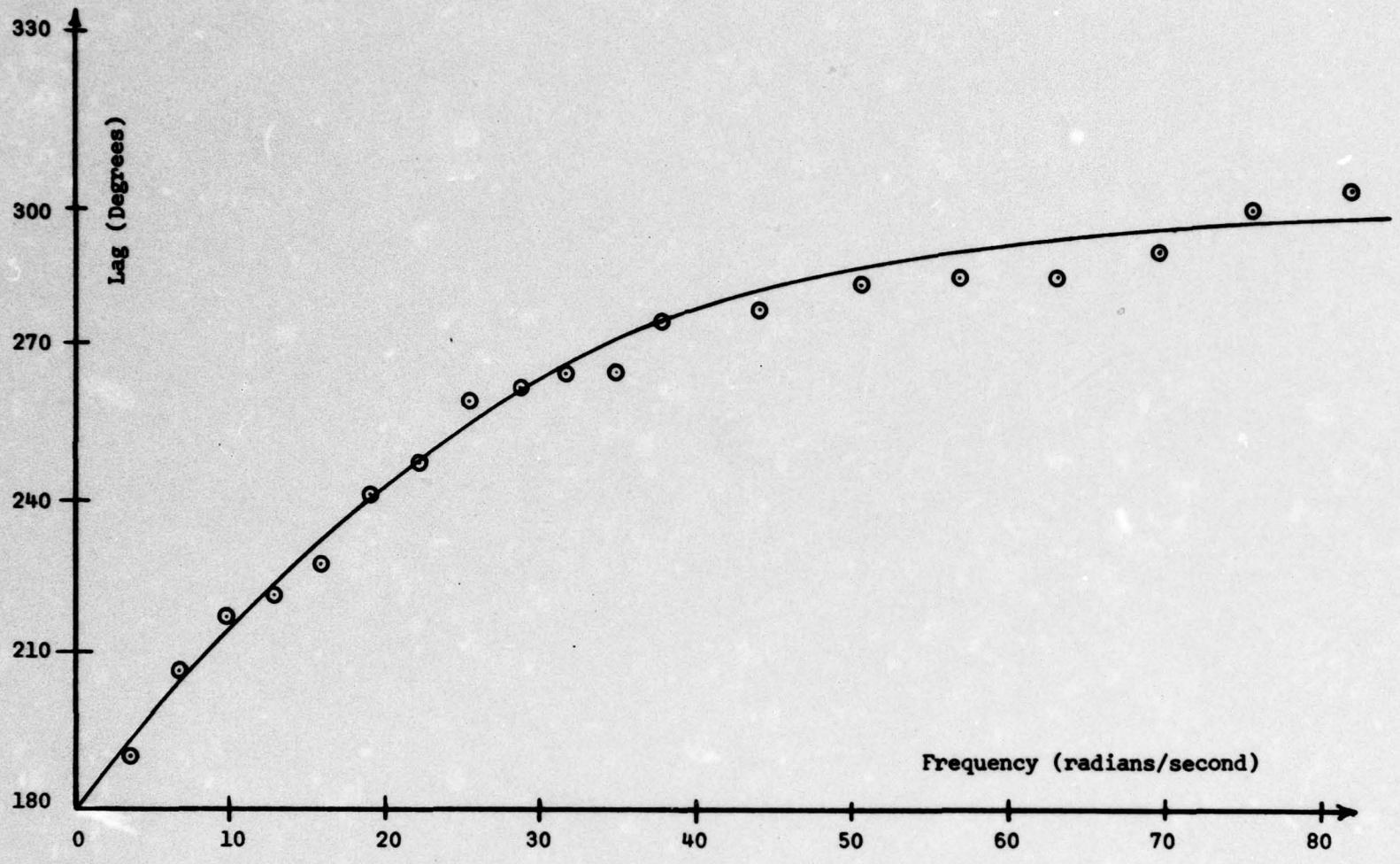

Figure 4. Phase Lag of Tail Pitch Behind Servo Amp Signal (Hydraulic Lag).

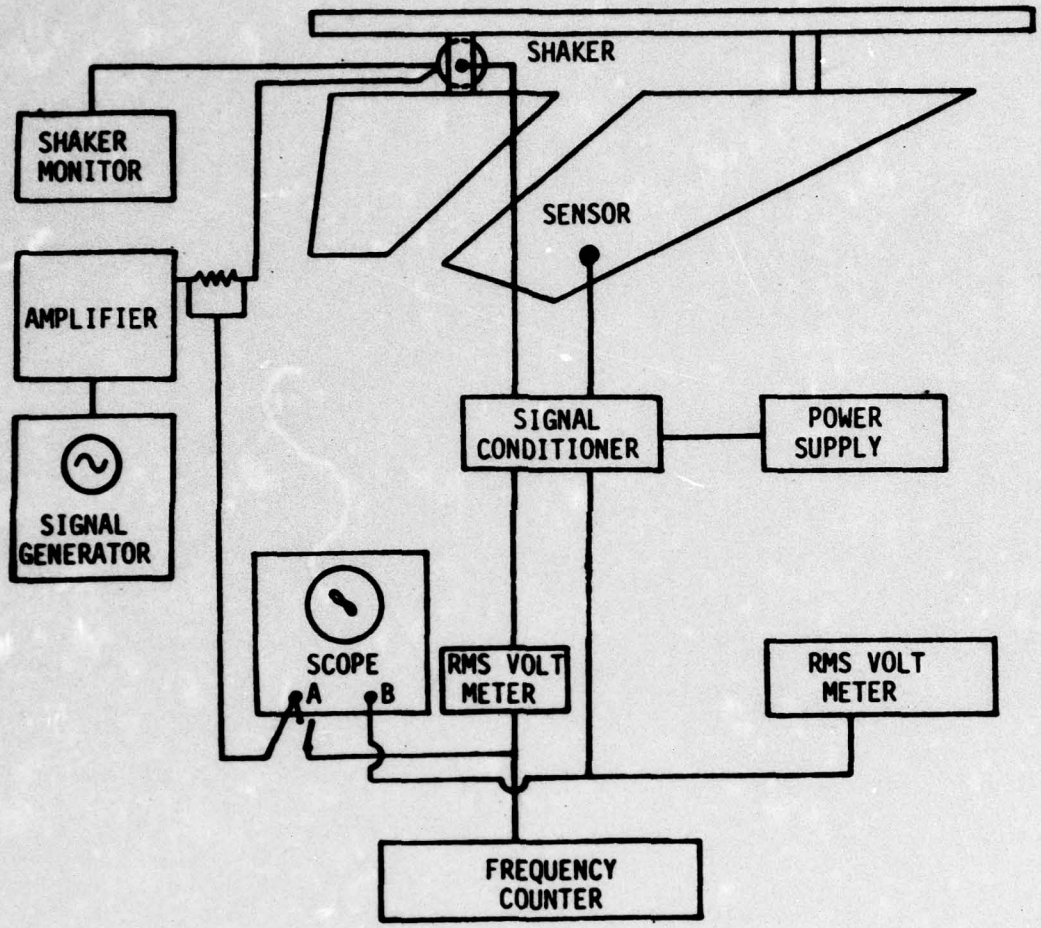

Figure 5. Schematic Diagram of Experimental Modeshape Measurement

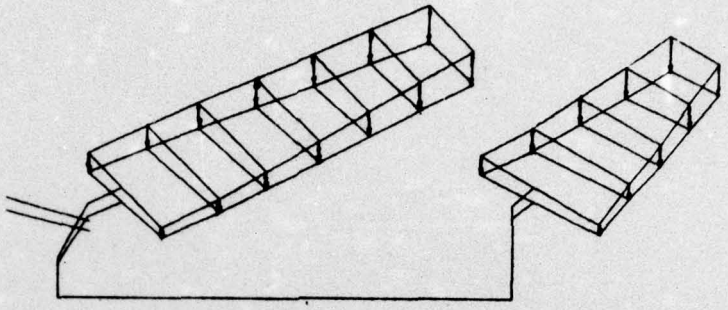

Mode 1, ω = 1.06 cps

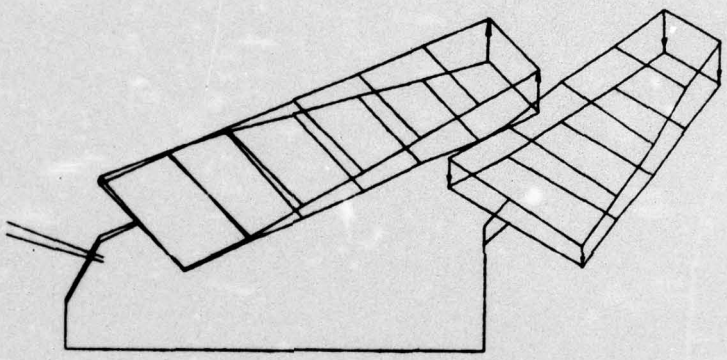

Mode 2, ω = 5.00 cps

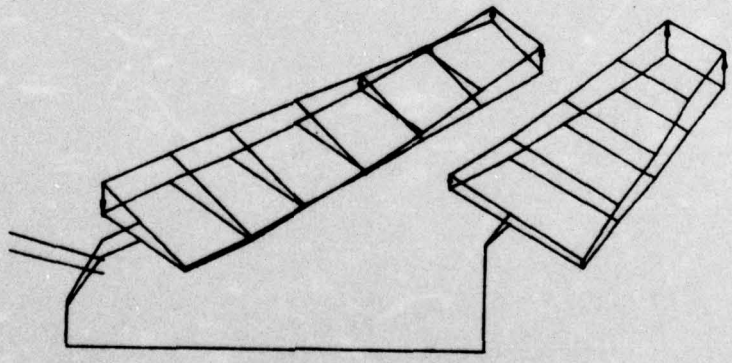

Mode 3, ω = 7.91 cps

Figure 6. Experimental Mode Shapes

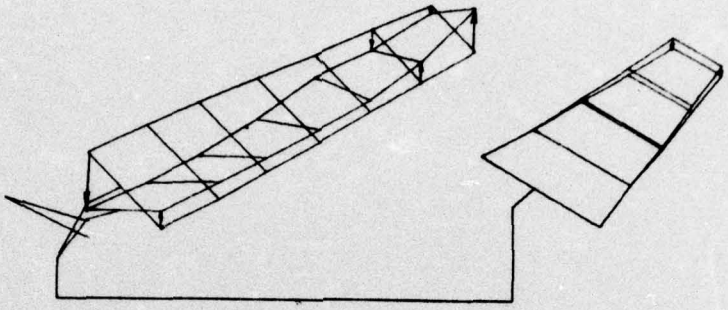

Mode 4, ω = 10.81 cps

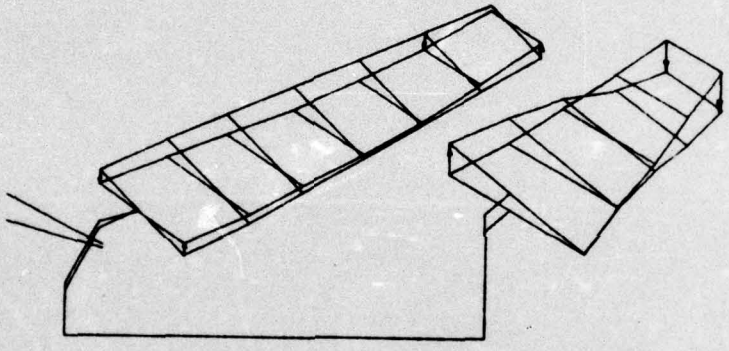

Mode 5, ω = 17.83 cps

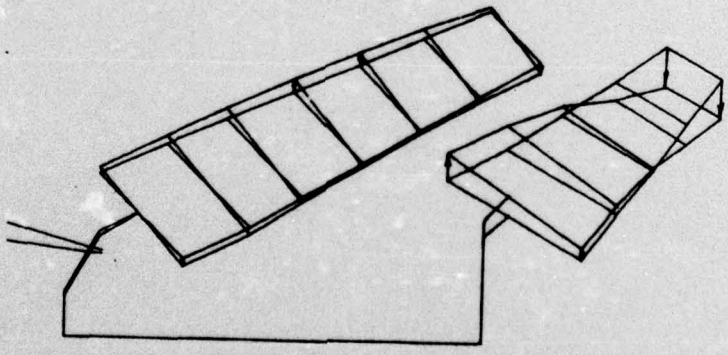

Mode 6, ω = 19.88 cps

Figure 6 (continued). Experimental Mode Shapes

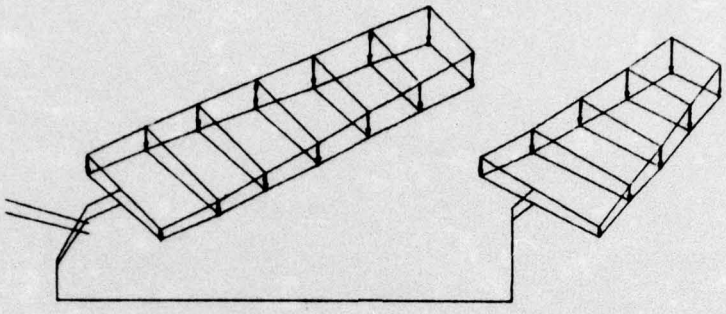

Mode 1, ω = 1.06 cps

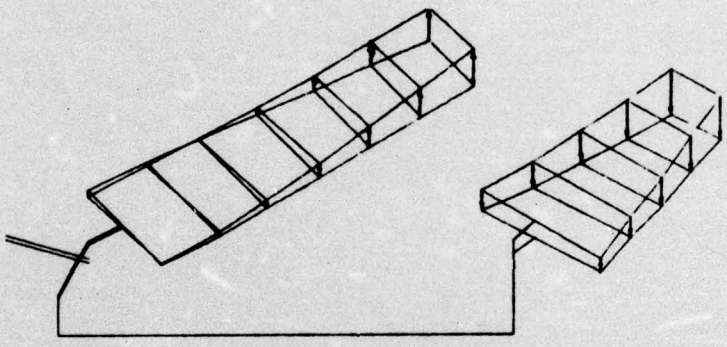

Mode 2, ω = 3.26 cps

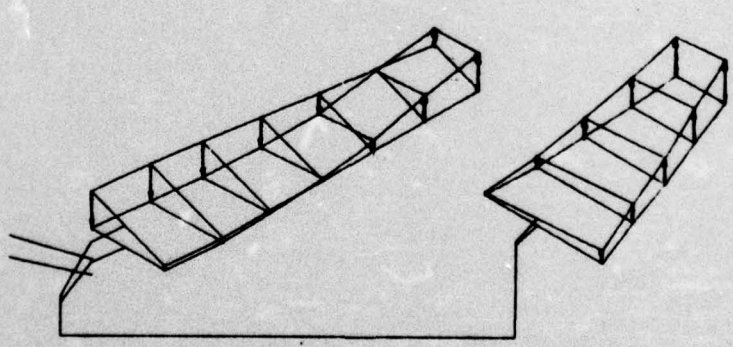

Mode 3, ω = 7.00 cps

Figure 7. Calculated Mode Shapes

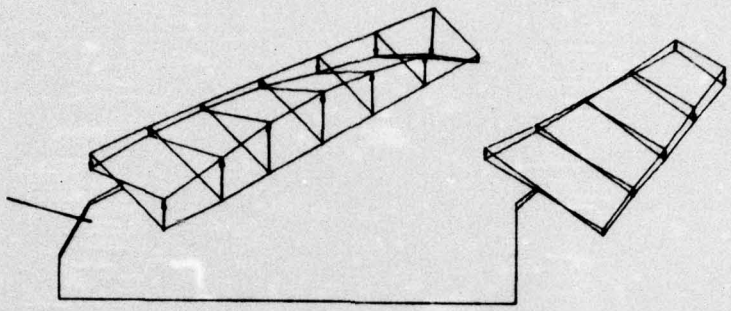

Mode 4, ω = 12.42 cps

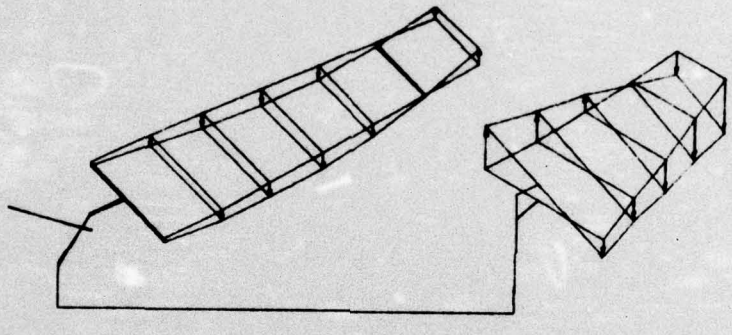

Mode 5, ω = 14.17 cps

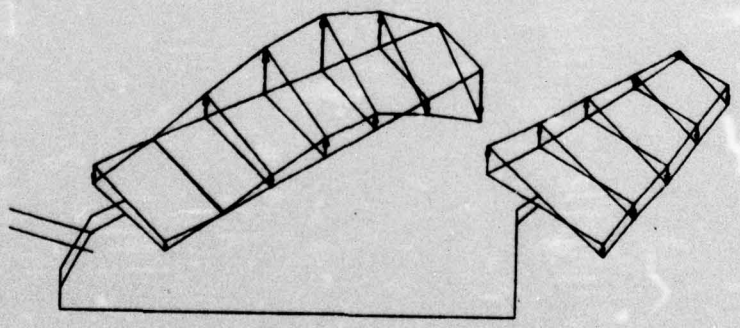

Mode 6, ω = 19.88 cps

Figure 7 (continued). Calculated Mode Shapes

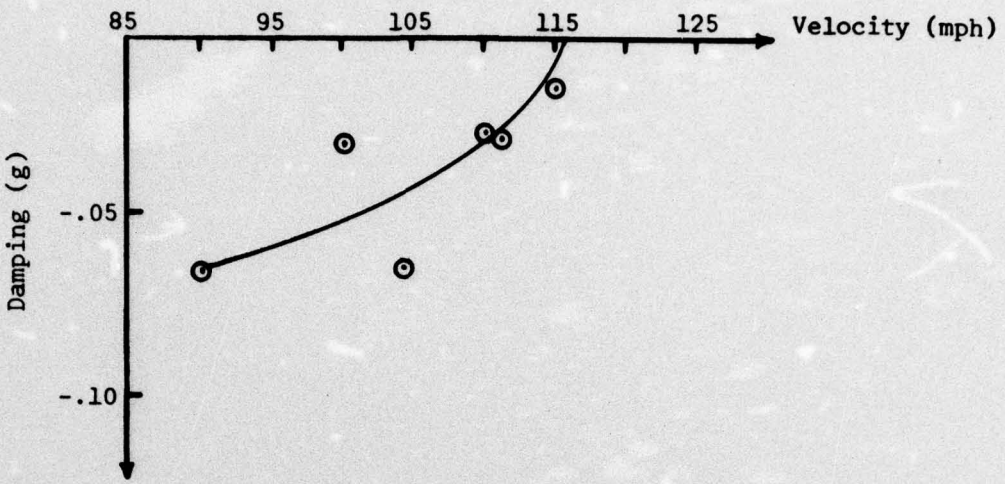

Figure 8. Experimental V-g Plot 60° Wing Sweep

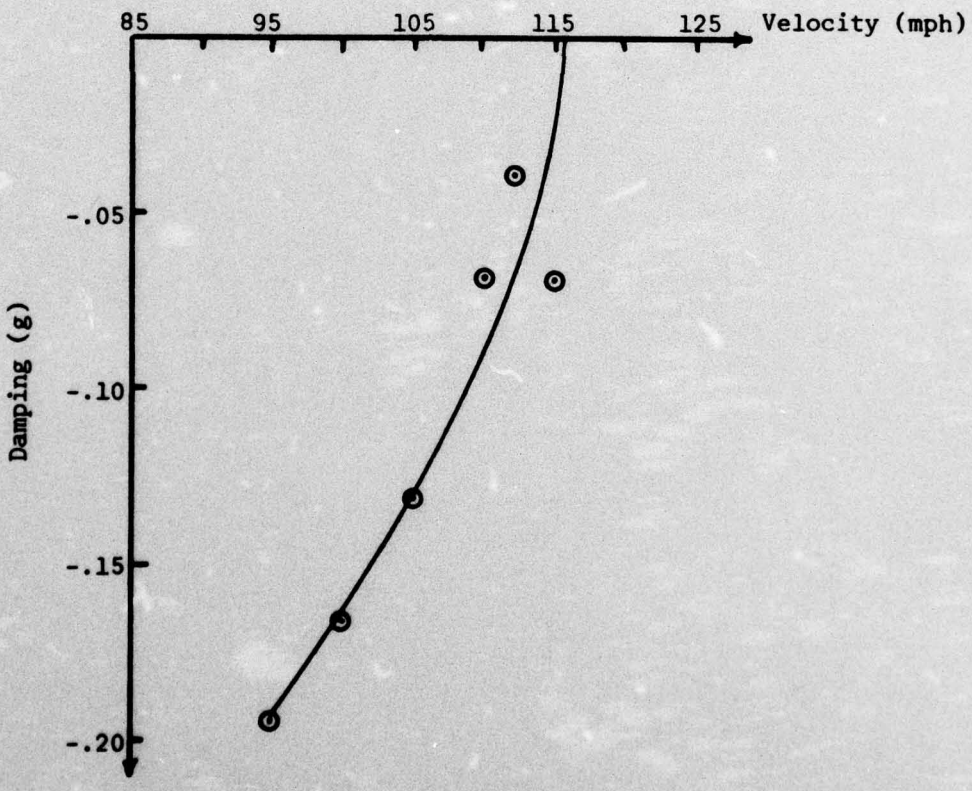

Figure 9. Experimental V-g Plot 45° Wing Sweep

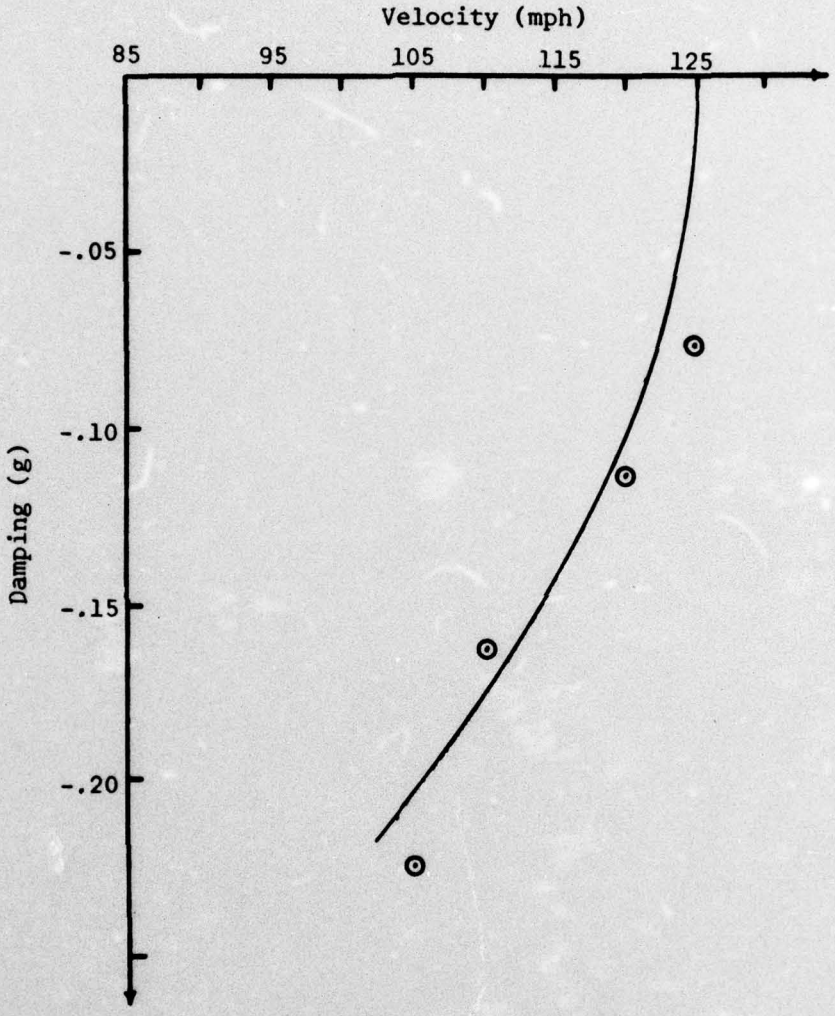

Figure 10. Experimental V-g Plot 30° Wing Sweep

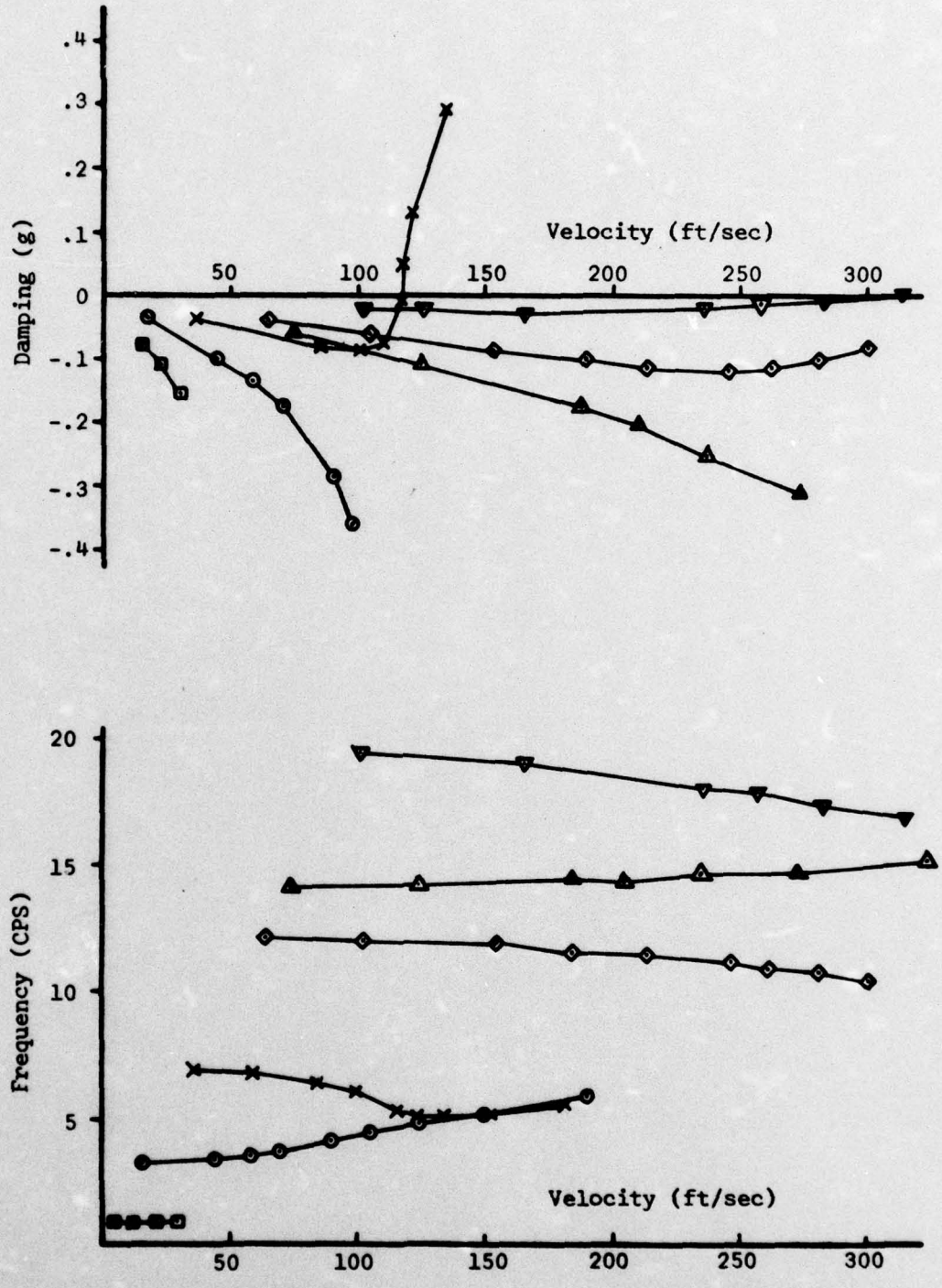

Figure 11. Analytical V-g and Frequency Plots; Passive Response; 60° Wing Sweep.

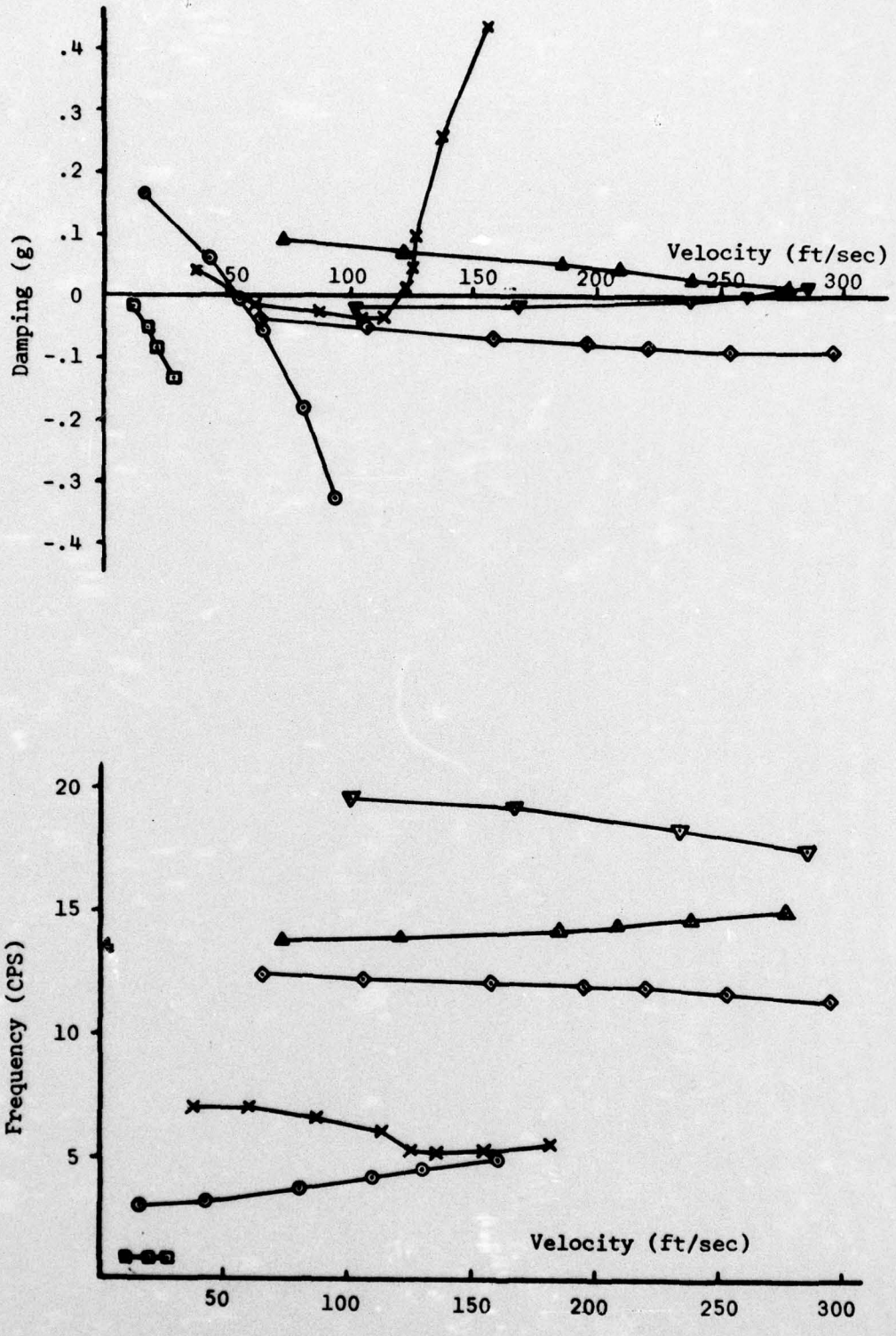

Figure 12. Analytical V-g and Frequency Plots; Feedback Controls Active; 60° Wing Sweep.

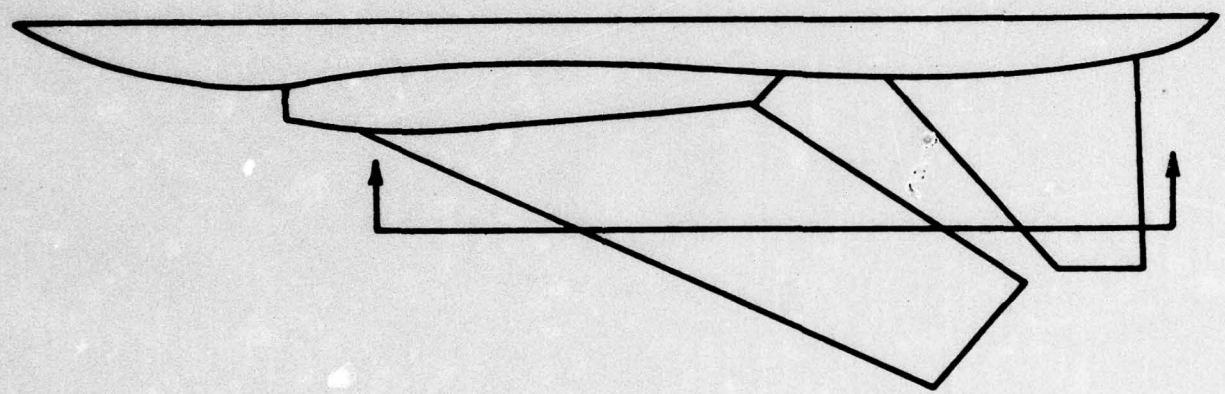

Figure 13. Aerodynamic Cross Section Shown in Figure 14.

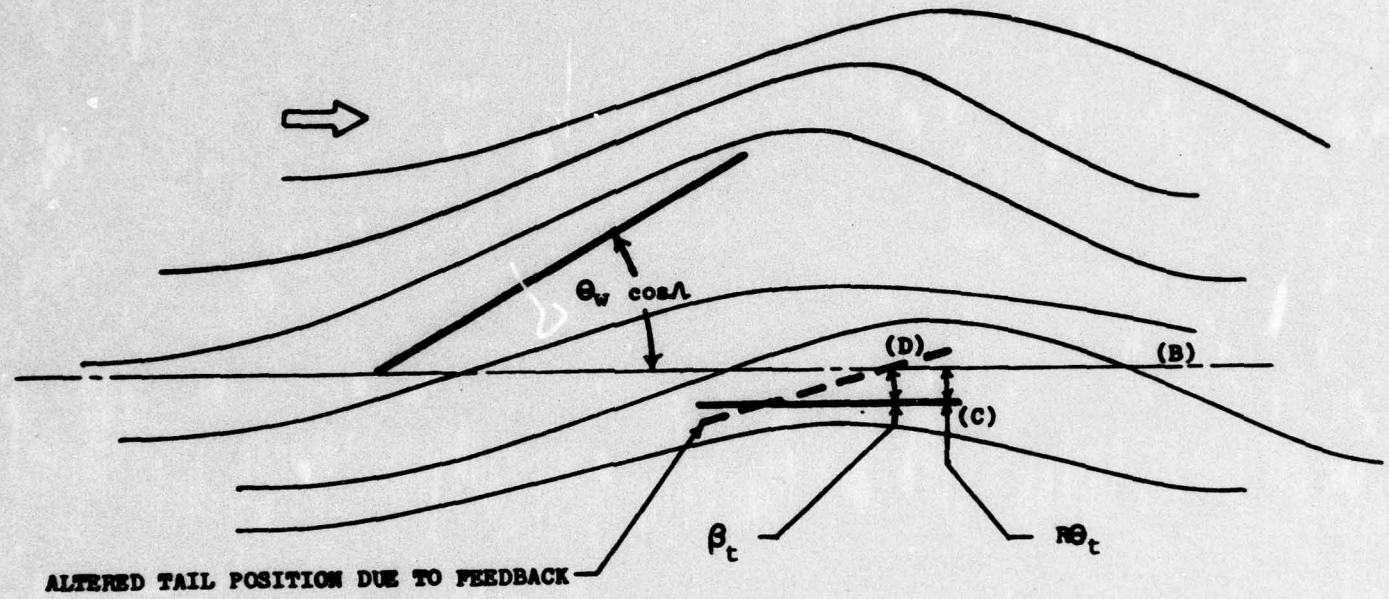

Λ = Wing sweep angle
R = Distance from central axis to typical section
θ_w = Wing flap angle
θ_t = Tail flap angle
β_t = Stabilator pitch angle

Figure 14. Typical section flow field for wing-tail flutter model.

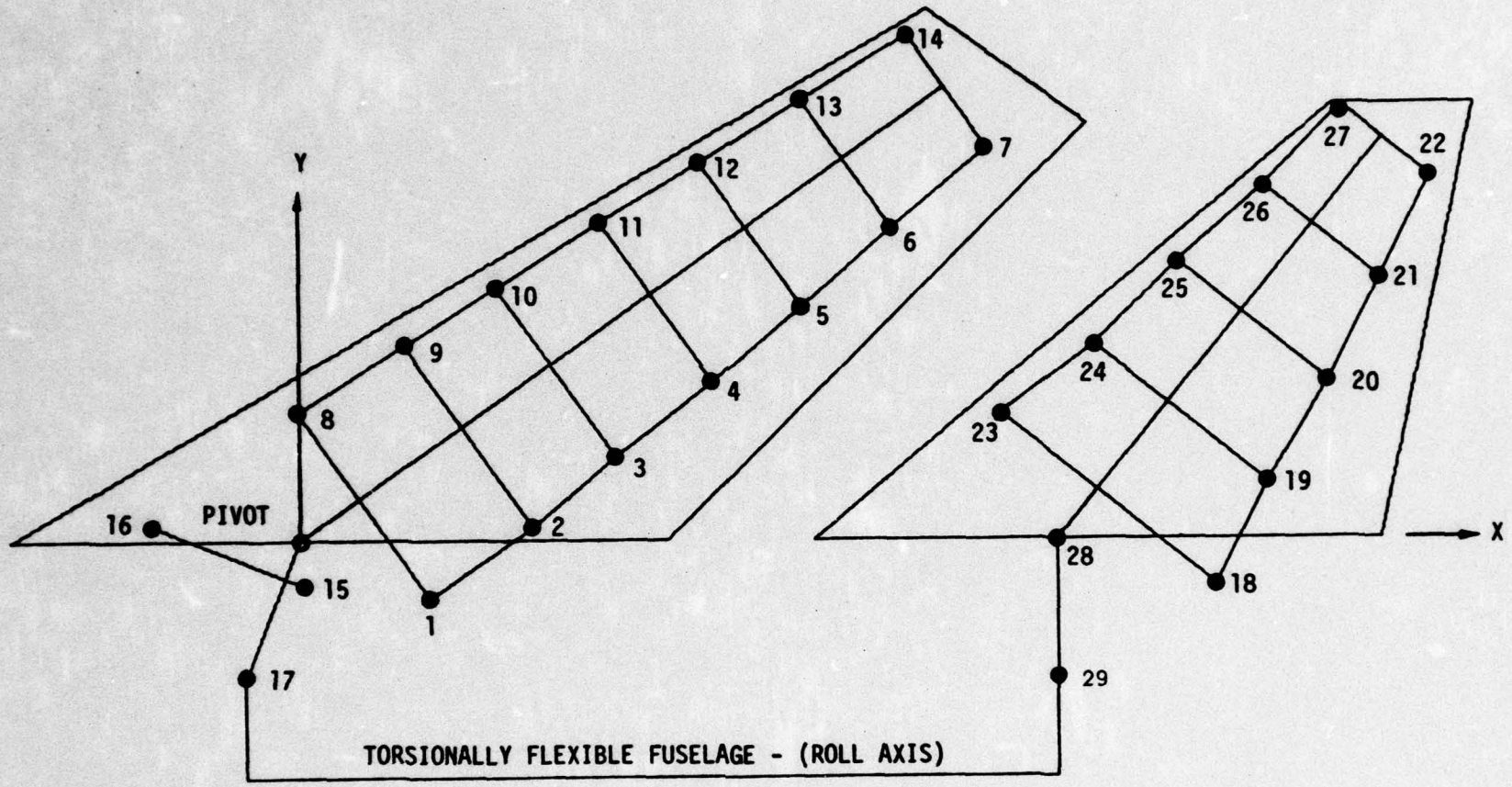

Figure 15. AFFDL 60° Dynamic Modeling

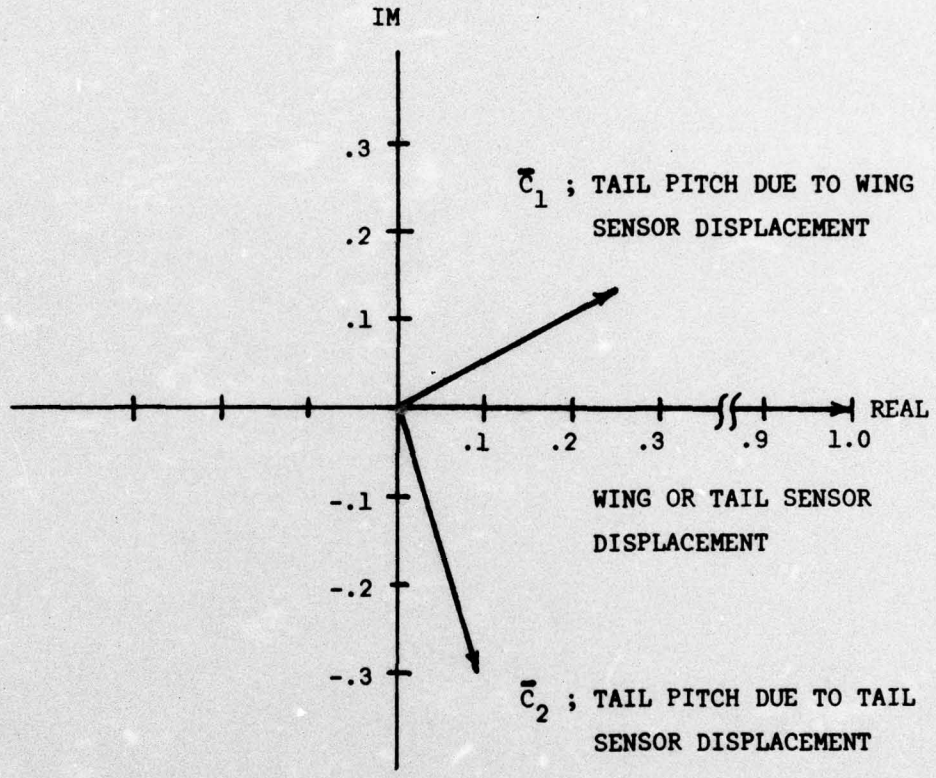

Figure 16. Graphic Representation of Control Law

Appendices

Appendix A

Statement of Problem

Because flutter prevention through the use of active controls uses both the techniques developed to determine aircraft flutter speeds and the methods developed for feedback control analyses, for clarity, it is beneficial to develop the basic equations of motion which are used to represent the response of a flexible aircraft and to relate these equations of motion to a basic feedback control analysis.

A.1 Basic Flexible Aircraft Response Equations

The response of a flexible aircraft to an external force is computed by solving a set of simultaneous equations obtained by applying Lagrange's equations of motion to the flexible aircraft. One of the most general developments of the response of a flexible aircraft is presented in reference 15 and the development of the equation of motion will follow this reference closely with supporting information being obtained from references 16, 9, and 17.

Lagrange's equations of motion for any structural dynamic system may be represented by

$$\frac{d}{dt}\left(\frac{\partial T}{\partial \dot{\bar{q}}_r}\right) - \frac{\partial T}{\partial \bar{q}_r} = \bar{Q}_r(t) \qquad r = 1,2,\ldots,n \qquad (A.1)$$

where

$\bar{q}_r$ is the r^{th} generalized coordinate

T is the kinetic energy

$\bar{Q}_r$ is the generalized force term associated with the r^{th} generalized coordinate.

The generalized force term $\bar{Q}_r$ is generally considered to be composed of three parts

$$\bar{Q}_r = \bar{Q}_{a_r} + \bar{Q}_{e_r} + \bar{Q}_{d_r} \tag{A.2}$$

where

$\bar{Q}_{a_r}$ is the force externally applied to the structure

$\bar{Q}_{e_r}$ is the internal elastic force

$\bar{Q}_{d_r}$ is the structural damping force

Since in most cases the elastic force can be derived from the strain energy potential then from Castigliano's theorem[13]:

$$\bar{Q}_{e_r} = - \frac{\partial U}{\partial \bar{q}_r} \tag{A.3}$$

where U is the strain energy potential.

With these definitions Equations (A.1) can be written in the form:

$$\frac{d}{dt}\left(\frac{\partial T}{\partial \dot{\bar{q}}_r}\right) - \frac{\partial T}{\partial \bar{q}_r} + \frac{\partial U}{\partial \bar{q}_r} - \bar{Q}_{d_r} = \bar{Q}_{a_r} \tag{A.4}$$

The terms in Equations (A.4) can be easily computed when these equations of motion are applied to an air vehicle's lifting surfaces and the following assumptions are made:

a. The only deformation of the lifting surfaces are deflections of the surface normal to their undeformed midplane.

b. The deflections of the surfaces are small such that the nonlinear structural terms associated with the change in curvature and the strain displacement relations can be neglected.

c. The only external forces on the structure are composed of differential aerodynamic pressures applied to the lifting surface (the differential aerodynamic pressures are the differences in pressure between the upper and lower portions of the surface).

d. The air vehicle is considered to be composed of planar surfaces.

The kinetic energy T can be expressed as:

$$T = \frac{1}{2} \int\int \bar{m}(x,y)\, \dot{f}^2(x,y,t)\, dx\, dy$$

where

$\bar{m}(x,y)$ is the mass distribution of the surface

$f(x,y,t)$ is the total deflection of the surface from the static equilibrium position

x,y is the coordinate system attached to the lifting surface

and where the integration is carried out over the entire lifting surface.

The deflection at any point on the lifting surface is found by taking a summation of the deflections at that point due to each of the generalized coordinates and the deflection of the control surfaces. This summation can be expressed as:

$$f(x,y,t) = \sum_{r=1}^{n} h_r(x,y)\, \bar{q}_r(t) + \sum_{j=1}^{m} h_{\delta_j}(x,y)\, \bar{\delta}_j(t) \qquad (A.5)$$

where

$h_r(x,y)$ is the deflection at point (x,y) on the lifting surface due to a unit value of the r^{th} generalized coordinate

$h_{\delta_j}(x,y)$ is the deflection of point (x,y) on the j^{th} control surface due to a unit deflection of the j^{th} control surface. It should be noted here that $h_{\delta_j}(x,y)$ is defined on the area of the j^{th} control surface and is zero on all other parts of the lifting surface

$\bar{\delta}_j(t)$ is the deflection of the j^{th} control surface. Note that $\bar{\delta}_j(t)$ is not a generalized coordinate in that the deflection of the control surface can be prescribed or when a feedback control system is used $\bar{\delta}_j(t)$ will be dependent on the $\bar{q}_r(t)$ generalized coordinates

m is the number of control surfaces

n is the number of generalized coordinates employed in the study.

The kinetic energy of the syttem can now be represented as:

$$T = \frac{1}{2}\iint \bar{m}(x,y)\left[\sum_{r=1}^{n} h_r(x,y)\,\dot{\bar{q}}_r(t) + \sum_{j=1}^{m} h_{\delta_j}(x,y)\,\dot{\bar{\delta}}_j(t)\right]\times \left[\sum_{s=1}^{n} h_s(x,y)\,\dot{\bar{q}}_s(t) + \sum_{i=1}^{m} h_i(x,y)\,\dot{\bar{\delta}}_i(t)\right] dx\,dy \tag{A.6}$$

Since the kinetic energy is a function of only $\dot{\bar{q}}_r(t)$ and not of $\bar{q}_r(t)$, the term

$$\frac{\partial T}{\partial \bar{q}_r} = 0$$

Now define

$$m_{rs} = \iint h_r(x,y)\,h_s(x,y)\,\bar{m}(x,y)\,dx\,dy \tag{A.6a}$$

and

$$m_{\delta_{rj}} = \iint h_r(x,y)\,h_{\delta_j}(x,y)\,\bar{m}(x,y)\,dx\,dy \tag{A.6b}$$

where the integration of the m_{rs} term is carried out over the entire lifting surface, but since $h_{\delta_j}(x,y)$ is zero except on the control surface the integration to determine the $m_{\delta_{rj}}$ term need only be carried out over only the j^{th} control surface. With this definition the $\frac{d}{dt}\left(\frac{\partial T}{\partial \dot{\bar{q}}_r}\right)$ term in the r^{th} equation of equations (A.4) may be written as

$$\frac{d}{dt}\left(\frac{\partial T}{\partial \dot{\bar{q}}_r}\right) = \sum_{s=1}^{n} m_{rs}\, \ddot{\bar{q}}_s(t) + \sum_{j=1}^{m} m_{\delta_{rj}}\, \ddot{\bar{\delta}}_j(t) \qquad (A.7)$$

At this point it should be noted that Equation (A.7) can be used for any generalized coordinate system. If orthogonal coordinates are used or more specifically, if the natural mode shapes of the lifting surface structure are used then

$$m_{rs} = 0 \quad \text{for} \quad r \neq s$$

The work, W, done on a thermally isolated system by slowly applied external forces is equivalent by the first law of thermodynamics to the strain energy, U, in the system and can be expressed as:

$$U = W = \frac{1}{2}\int\int P_t(x,y,t)\, f(x,y,t)\, dx\, dy \qquad (A.8)$$

where $P_t(x,y,t)$ is the total force acting on the structure and $f(x,y,t)$ is the total deflection of the structure from the static equilibrium position. The expression for the strain energy can be put into a more useful form if the total force is written in terms of the deflections:

$$P_t(x,y,t) = \iint K(x,y,\xi,\eta)\, f(\xi,\eta,t)\, d\xi\, d\eta \qquad (A.9)$$

where $K(x,y,\xi,\eta)$ is the structural stiffness influence function. The strain energy of the structure now becomes:

$$U = \frac{1}{2}\iint f(x,y,t) \iint K(x,y,\xi,\eta)\, f(\xi,\eta,t)\, d\xi\, d\eta\, dx\, dy \qquad (A.10)$$

By substituting the series expression for the deflection at any point and defining

$$K_{rs} = \iiiint h_r(x,y)\, K(x,y,\xi,\eta)\, h_s(\xi,\eta)\, d\xi\, d\eta\, dx\, dy \qquad (A.11)$$

the strain energy may be written as:

$$U = \frac{1}{2} \sum_{r=1}^{n} \sum_{s=1}^{n} \bar{q}_r(t)\, \bar{q}_s(t)\, K_{rs} \qquad (A.12)$$

Using this definition of the potential energy the $\frac{\partial U}{\partial \bar{q}_r}$ term of the r^{th} equation of Equation (A.4) becomes

$$\frac{\partial U}{\partial \bar{q}_r} = \sum_{s=1}^{n} K_{rs}\, \bar{q}_s(t) \qquad (A.13)$$

If the natural mode shapes are used as the generalized coordinates then

$$K_{rs} = 0 \quad \text{for} \quad r \neq s$$

and the well known relationship between the free vibration frequency, mass, and stiffness

$$K_{rr} = \omega_r^2\, m_{rr}$$

can be used.

Structural damping is due to internal friction within a structure or at the connections between elements of a structural system. The resulting damping forces are a function of the strain, or deflections in the structure. For an elastic system, undergoing simple harmonic motion, the r^{th} structural

damping force may be assumed to be proportional in magnitude to the internal elastic force and opposite in direction to the velocity vector. Therefore, for a structure undergoing harmonic motion, the structural damping force is usually expressed as:

$$-\bar{Q}_{d_r} = i\, g \sum_{s=1}^{n} K_{rs}\, \bar{q}_s(t) \qquad (A.15)$$

where g, the proportionality constant, is called the structural damping factor and i is the unit imaginary number [16,9].

When the external forces applied to the structure are forces due only to the differential aerodynamic pressures, the applied external force term associated with the r^{th} generalized coordinate can be defined as:

$$\bar{Q}_{A_r}(t) = \iint h_r(x,y)\, P_E(x,y,f,t)\, dx\, dy \qquad (A.16)$$

where $P_E(x,y,f,t)$ is the total external pressure on the lifting surface. If the deflections are small (within the range of linear aerodynamics) the pressure differential can be written as the sum of three different pressure distributions

$$P_E(x,y,f,t) = P(x,y,f,t) + \bar{W}_g(t)\ \bar{P}_F(x,y,t) + \bar{P}_{\delta_j}(x,y,t)\bar{\delta}_j(t) \qquad (A.17)$$

where

$P(x,y,f,t)$ is the differential pressure arising from the deflection and motion of the lifting surface

$\bar{W}_g(t)$ is an aerodynamic flow disturbance such as a wind gust

$\bar{P}_F(x,y,t)$ is the differential pressure distribution arising from a unit value of the aerodynamic flow disturbance

$\bar{P}_{\delta_j}(x,y,t)$ is the differential pressure distribution caused by a unit deflection of the j^{th} control surface

$\bar{\delta}_j(t)$ is the deflection of the j^{th} control surface

Since $P(x,y,f,t)$ is a function of the motion of the lifting surface, this system is a force feedback system, even without any feedback controls, in that the externally applied forces are a function of the motion of the system. For the present it will be assumed that the pressure distribution due to the motion of the lifting surface can be expressed in the general form:

$$P(x,y,f,t) = \sum_{s=1}^{n} \bar{q}_s(t) \; \bar{P}_s(x,y,t) \qquad (A.18)$$

where $\bar{P}_s(x,y,t)$ is the pressure distribution due to a unit amount of the s^{th} generalized coordinate. Equation (A.18) indicates that the pressure is proportional to the displacement. Actually, the pressure distribution is a function of the displacement and velocity of the lifting surface normal to the undeformed position along with the velocity, density, and Mach number of the airstream passing over the lifting surface. However, for clarity at this point in the development of the equations of motion, Equation (A.18) can be used to represent the pressure distribution until a specific aerodynamic method is used in the computation of the

aerodynamic pressure. Now by defining:

$$\bar{Q}_{rs} = \iint h_r(x,y)\, \bar{P}_s(x,y,t)\, dx\, dy \tag{A.19}$$

$$\bar{Q}_{F_r} = \iint h_r(x,y)\, \bar{P}_F(x,y,t)\, dx\, dy \tag{A.20}$$

$$\bar{Q}_{\delta_{rj}} = \iint h_r(x,y)\, \bar{P}_{\delta_j}(x,y,t)\, dx\, dy \tag{A.21}$$

the $\bar{Q}_{A_r}$ term in the r^{th} equation of Equation (A.4) becomes

$$\bar{Q}_{A_r} = \sum_{s=1}^{n} \bar{q}_s(t)\, \bar{Q}_{rs} + \bar{W}_g \bar{Q}_{F_r} + \sum_{j=1}^{m} \bar{\delta}_j(t)\, \bar{Q}_{\delta_{rj}} \tag{A.22}$$

Now using the above definitions for all the terms in Equation (A.4) and placing all the known or specified terms on the right hand side of the equation, Equation (A.4) becomes:

$$\sum_{s=1}^{n} m_{rs}\, \ddot{\bar{q}}_s(t) + (1 + ig) \sum_{s=1}^{n} K_{rs} \bar{q}_s(t) - \sum_{s=1}^{n} \bar{q}_s(t)\, \bar{Q}_{rs}$$

$$= - \sum_{j=1}^{m} m_{\delta_{rj}}\, \ddot{\bar{\delta}}_j(t) + \sum_{j=1}^{m} \bar{Q}_{\delta_{rj}} \bar{\delta}_j(t) + \bar{Q}_{F_r} \bar{W}_g(t) \tag{A.23}$$

$$(r = 1, 2, \ldots n)$$

Equation (A.23) is a very general equation describing the dynamic response on an air vehicle due to known forcing functions $\bar{W}_g(t)$ and $\bar{\delta}(t)$.

One of the greatest difficulties in the solution of Equation (A.23) is the computation of the aerodynamic force terms. At the present time no general method of computing the strictly unsteady aerodynamic force terms for a lifting surface has been developed. However, recently developed computer programs can accurately predict the unsteady aerodynamic forces on complex aircraft lifting surfaces which are oscillating harmonically in time[18, 10]. Therefore, when harmonic motion is assumed of the form:

$$\bar{q}_r(t) = q_r e^{i\omega t} \tag{A.24}$$

where q_r is complex, the pressure distribution due to the r^{th} mode becomes:

$$\bar{P}_r(x,y,t)\bar{q}_r(t) = P_r(x,y,\omega)\, q_r e^{i\omega t} \tag{A.25}$$

where $P_r(x,y,\omega)$ is complex.

In actual practice, the aerodynamic pressure distribution is computed as a function of the reduced frequency (k) which is defined as:

$$k = \omega b/V \tag{A.26}$$

where

- ω is the frequency of oscillation of the lifting surface
- V is the velocity of the airstream passing over the lifting surface
- b is a reference length which is usually either the semi-span or semi-chord of the lifting surface.

Since the aerodynamic pressure distribution at a given reduced frequency

varies only with the Mach number and since the coefficients of pressure can be computed for a single Mach number without specifying the altitude or air stream velocity the pressure force is usually defined as:

$$P_s(x,y,k) = 1/2\ \rho V^2 \Delta C_{p_s}(x,y,k,M) \tag{A.27}$$

where

$\Delta C_{p_s}(x,y,k,M)$ is the coefficient of pressure due to a unit value of the s^{th} generalized coordinate and at a specified reduced frequency (k) and Mach number (M)

ρ is the air density

V is the free stream velocity

Now defining

$$Q_{rs} = \int\int h_r(x,y)\ \Delta C_{p_s}(x,y,k,M)\ dx\ dy \tag{A.28}$$

$$Q_{\delta_{rj}} = \int\int h_r(x,y)\ \Delta C_{p_{\delta_j}}(x,y,k,M)\ dx\ dy \tag{A.29}$$

$$Q_{F_r} = \int\int h_r(x,y)\ \Delta C_{p_F}(x,y,k,M)\ dx\ dy \tag{A.30}$$

Equation (A.23) becomes:

$$\sum_{s=1}^{n} \left[m_{rs} - \frac{(1+ig)}{2} K_{rs} + 1/2\ \frac{\rho b^2}{k^2} Q_{rs} \right] q_s(\omega)$$

$$= - \sum_{j=1}^{m} \left[m_{\delta_{rj}} + 1/2\ \frac{\rho b^2}{k^2} Q_{\delta_{rj}} \right] \delta_j(\omega) - 1/2\ \frac{b^2 \rho}{k^2} Q_{F_r} W_g(\omega) \tag{A.31}$$

$$(r = 1, 2, \ldots n)$$

where both sides of the equation have been divided by $-\omega^2 e^{i\omega t}$ and where the relationship $k = \frac{\omega b}{V}$ has been used.

Appendix B

Wind Tunnel Model Design[5]

As mentioned earlier, the basic model employed in this study is a variation on the AFFDL wing-tail flutter model designed by the Air Force Flight Dynamics Laboratory and discussed in reference 4. Some of the model design details were modified by personnel at The University of Texas at Austin to include an active stabilator control in pitch and a remote control of the wing sweep angle. This model is illustrated in Figure 1. The model degrees of freedom include a rigid body roll mode, wing root bending and torsional flexibilities, fuselage torsional flexibility, and fully flexible wing and stabilator modes. In addition, the stabilator could be remotely pitched by means of a hydraulic actuator to provide a stiff control degree of freedom. The wing could also be remotely swept with a hydraulic actuator to simulate various geometries as well as rapidly convert the flutter model to a stable configuration by quickly sweeping the wing forward, raising the system's flutter speed. This latter feature was added with the hope that in some cases it could suppress undesirable model responses that may occur during critical flutter conditions.

A schematic of the model's hydraulic control supply system, employed to activate both wing sweep and stabilator motions, is illustrated in Figure B.1. This control system is comprised of three major assemblies: the hydraulic power supply module, the servo control module,

and the model hydraulic actuator system designated respectively as (a), (b), and (c) in the schematic. These components are also illustrated in Figure B.2. The hydraulic power supply module is built around an Everpac Model PA-101 air driven hydraulic pump obtained without charge from government surplus. The pump provides a flow of 7.647 cm^3/sec (0.467 in^3/sec) at 690 N/cm^2 (1000 psi) which is the normal working pressure of the system. Due to the relatively small capacity of the self-contained reservoir within the pump, an additional reservoir was installed in the hydraulic return line. The hydraulic power supply module also provides, to both the wing sweep system and the stabilator sweep system, backup accumulators charged to 345 N/cm^2 (500 psi) with nitrogen. These accumulators further serve to attenuate fluctuations in line pressure caused by pulsations of the pump or head pressure.

The servo control modules are mounted atop and outside the wind tunnel next to the model to minimize line lag effects to the model control actuators. This module provides terminal points for the servovalve electronics and houses two surplus Moog Model 971A servovalves rated at 18.03 cm^3/sec (1.1 in^3/sec) at 8 mA. These servovalves are employed to activate two Clippard Minimatic 7DD-1 double-acting actuators driving the wing sweep and stabilator motions. One end of the actuator rods is attached to a linear variable differential transformer (LVDT) which provides for precise control of the stabilator pitch and wing sweep angle while the other end drives the linkage motion. Signals to the wing sweep servoamplifier include the wing

sweep control signal, position feedback from the wing sweep LVDT, and a dither signal to keep the valve free of sediment and improve transient response. Signals to the stabilator pitch servoamplifier include the conditioned transducer signals, position feedback from the stabilator pitch LVDT, and the dither signal.

The control feedback avionics, developed as a part of the flutter suprression system, are illustrated in Figure B.3. An analog control was developed due to the expense and complexity of digital systems. The avionics for the stabilator pitch control include printed circuit modules for input control and amplification, integration, and phase shifting. It allows for up to three channels of output which can command up to three separate aerodynamic surfaces. The unit can monitor signals from accelerometers, velocity pickups, and/or strain gages mounted at select positions on the model and blend these according to a preselected control law. The modular grouping of the different circuits in this manner permits the programming of a variety of control laws.

Chains of inexpensive high-input impedance operational amplifiers, which constitute the basic elements of analog computers, were put together to perform the required control functions. EGC 941 M op amps were first breadboarded into functional blocks and tested to determine component values for best performance. Continuing the concept of functional blocks, modular construction was adopted in the layout of the model control panel thus enabling quick replacement of defective circuits and testing on a modular basis. Other benefits of modular

construction were realized including ease in circuit modification and construction, as well as circuit substitution if desired.

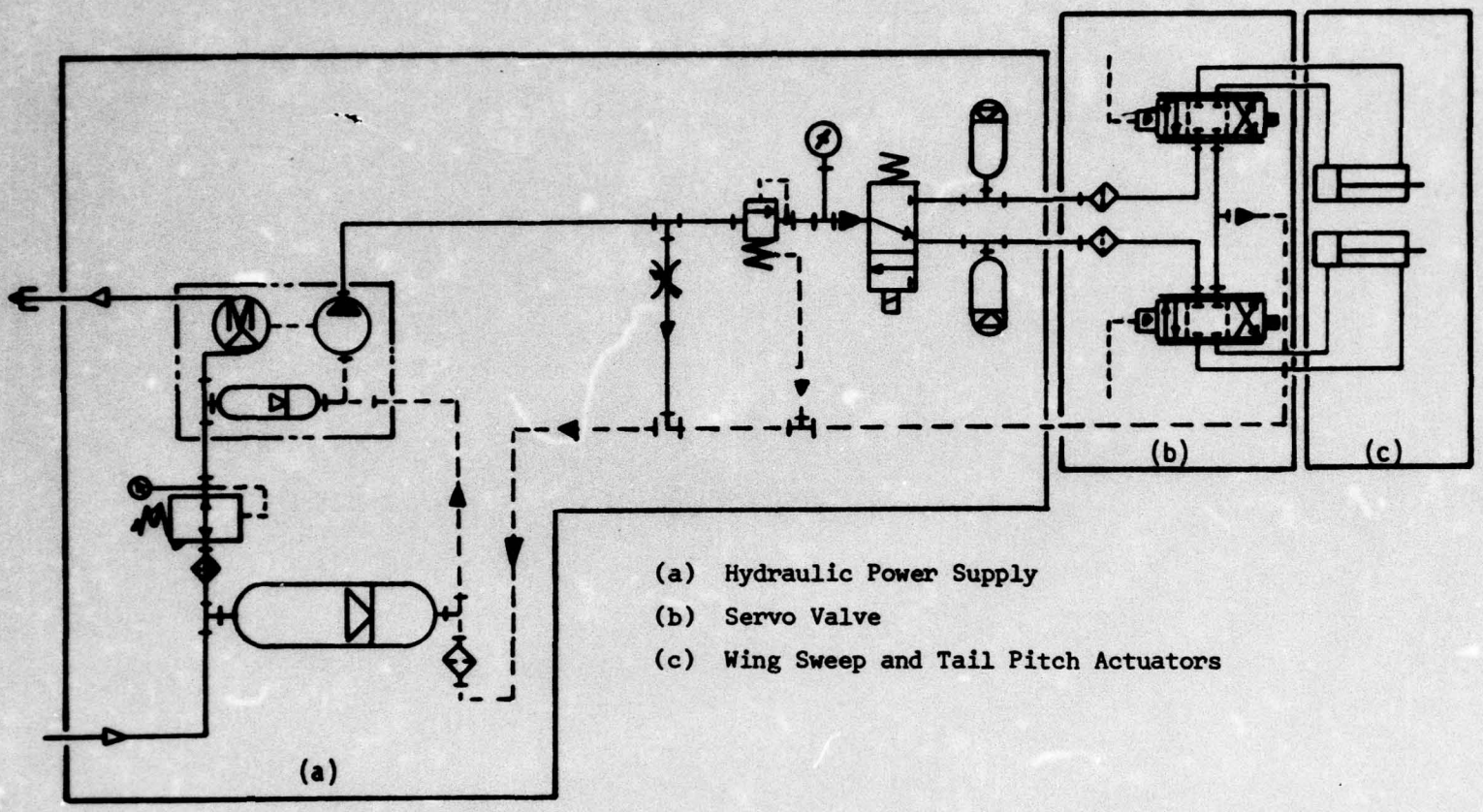

(a) Hydraulic Power Supply

(b) Servo Valve

(c) Wing Sweep and Tail Pitch Actuators

Figure B.1. Schematic Diagram of Hydraulic Systems.

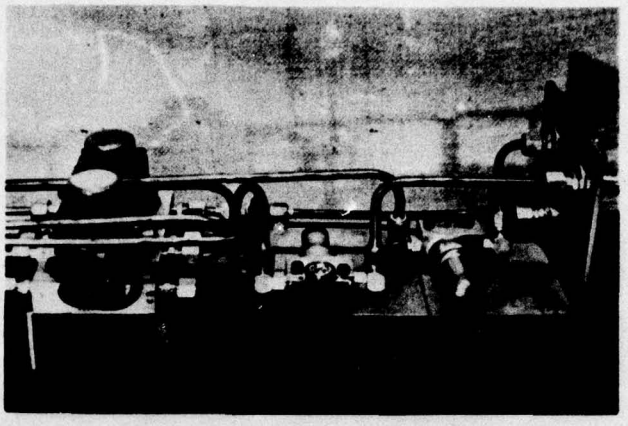

Servovalves

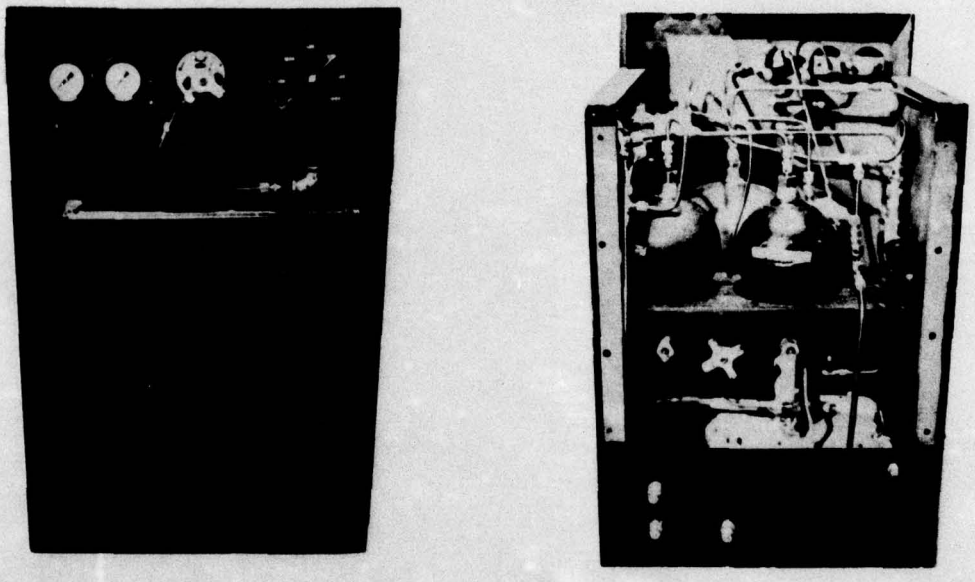

Hydraulic power supply

Figure B.2. Hydraulic Power Supply and Servovalves for Modified AFFDL Wing-Tail Flutter Model.

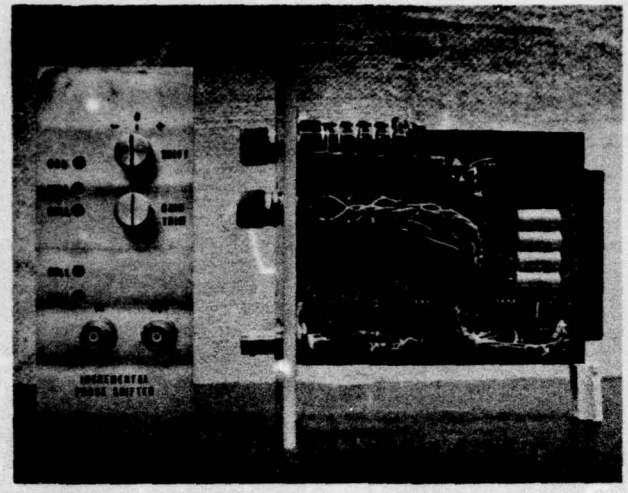

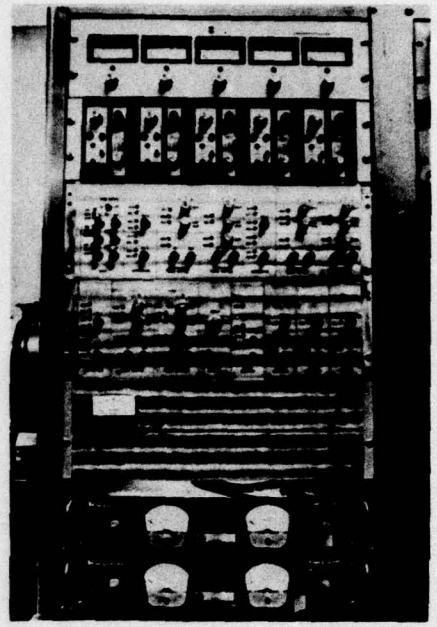

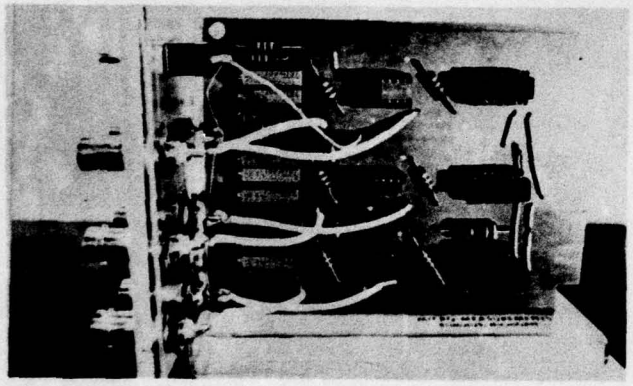

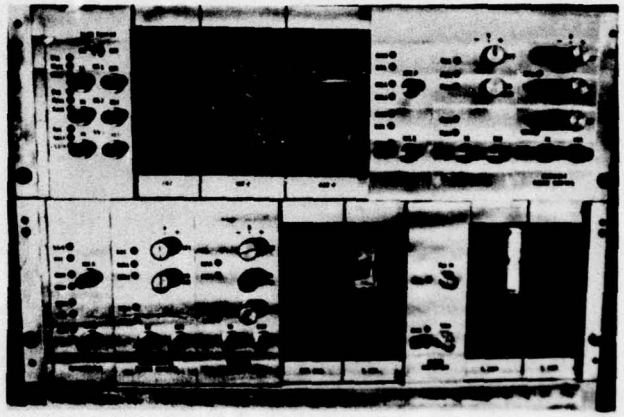

Figure B.3. Control Feedback Avionics for Modified AFFDL Wing-Tail Model. Small operational amplifiers illustrated along with modular units for performing various required control functions.

Appendix C

Dynamic System Identification

C.1 Procedure for Measurement of Mass and Inertia Properties

C.1.1 Mass Measurements

The wing consists of seven sections and the tail five sections (Figs. 1 and C.1) which can be detached separately from the spar. These sections are weighed separately. The weight contribution from the spar to each section is added to find total section weight.

C.1.2 Static Unbalance for Wing and Tail

Each section is supported at its spar center line on a knife edge. The force necessary to ballance the section is then measured by an accurate weighing scale. The product of this force and the balancing moment arm gives the static unbalance (Fig. C.2).

C.1.3 Inertia Measurements

The experimental determination of the mass moment of inertia consists of supporting the surface by a knife edge on the spar center line with the trailing edge supported by two springs of known constants k_1 and k_2 (Fig. C.3). The section is perturbed and the period of oscillation measured. The spring moment arm is also measured. The section inertia about the spar centerline is calculated from the equation

$$I = \frac{D^2 (k_1 + k_2)}{\omega^2} - \frac{Wx}{\omega^2} \qquad (C.1)$$

where:

I = section inertia about spar center line

D = distance from support point to spring attachment

k_1, k_2 = spring stiffnesses

ω = frequency of oscillation

W = weight of section

The inertia of the wing carry through about the pitch axis was similarly measured.

The inertia of the forward and aft fuselage components about the model roll axis were also measured. The procedure is to measure the pendulum frequency and then the angular deflection, Θ , for a known force (Fig. C.4). If Θ is small the roll inertia may be calculated by:

$$I_r = \frac{F \cdot d}{\sin \Theta \cdot \omega^2} \qquad (C.2)$$

where

I_r = fuselage sections roll inertia

ω = pendulum frequency

F = applied force

Θ = deflection angle

d = distance from roll axis to force

C.2 Flexibility and Torsion Coefficient Measurement for Wing and Tail Spars

To determine the spar bending flexibilities the spar is rigidly clamped as shown in Figure C.5. A load is applied at a section attachment point and the deflection measured at that and all other section attachment points on the spar. The F_{ij} element of the bending flexibility is the displacement of the i^{th} station for unit force at the j^{th} station. The procedure is repeated with the load applied at each station. In the present definition the whole procedure was performed twice with a different load in each case. The average of the two flexibilities was used. The symmetry check of the spar flexibility matrix was good. The values agreed to four decimal places.

The spar torsional flexibility influence coefficients are measured much the same way. A torque is applied at a section station with the angular deflections at each station measured. The T_{ij} element is the angular displacement at the i^{th} station due to a torque at the j^{th} station. Again, the averaging technique was used and good symmetry agreement was achieved.

C.3 Procedure for Assembly of Flexibility and Mass Matrices

I. Mass Matrix

A. Wing and Tail Section Masses

1. Weigh each section (seven wing and five tail sections)

2. Divide each section mass into two lump masses

a. Measure static unbalance

b. Measure moment of inertia

c. Calculate positions of lump masses (Position along spar will be abeam section c.g.)

1) Calculate distance of lump masses from spar center line preserving both static unbalance and mass moment of inertia

a) D1=section static unbalance/section mass

b) D2=section moment of inertia/section mass

c) Position of one lump mass ahead of spar center line, perpendicular to spar centerline:

$P1=D1+(D2-D1^2)^{1/2}$

d) Position of second lump mass aft of spar center line, perpendicular to spar centerline:

$P2=D1-(D2-D1^2)^{1/2}$

B. Wing and Tail Carry Throughs and Fuselage

1. Measure forward fuselage roll inertia

2. Measure aft fuselage roll inertia

3. Weigh wing carry through outboard of roll spring

a. Divide into two lump masses and position in same manner as wing section lump masses

4. Determine equivalent forward fuselage mass and position

a. Position the equivalent mass at roll spring (excluding that mass measured in step 3)

b. Calculate magnitude of equivalent mass

M(17)=(forward fuselage roll inertia - carry through roll inertia)/(distance to roll axis)^2

5. Determine equivalent aft fuselage mass and position

a. Position the equivalent mass at intersection of tail root chord and tail carry through

b. M(28) = aft fuselage roll inertia/(distance to roll axis)^2

C.4 Procedure for Assembly of Flexibility Matrix

I. Measure Component Flexibilities

A. Measure wing spar bending flexibilities (KW(I,J),I,J=1,7)

1. KW(I,J) = deflection at point I due to unit load at point J

B. Measure Tail Spar Bending Flexibilities (KT(I,J),I,J=1,5)

C. Measure Wing Spar Torsion (TU(I,J),I=1,7)

1. TW(I,J) = rotation angle at I due to unit torque at J

D. Measure Tail Spar Torsion (TT(I,J),I,j=1,5)

E. Measure Pitch and Roll Spring and Fuselage Flexibilities

1. P = Pitch spring flexibility = angle of deflection due to unit moment

2. R = Roll spring flexibility = angle of deflection due to unit moment

3. f = Fuselage flexibility = angle of rotation due to unit torque

F. Measure Tail Pitch Flexibility (TPF)

G. Determine Moment Arm of Tail Mass Points to Tail Pitch Axis (TPD(J), J=18,28)

II. Assemble Flexibility Matrix (28 x 28)

A. Initialize the Bending Flexibility Matrix as Follows:

B. Initialize the Torsion Flexibility Matrix in Same Manner (T(I,J) with TW and TT in place of KW and KT respectively)

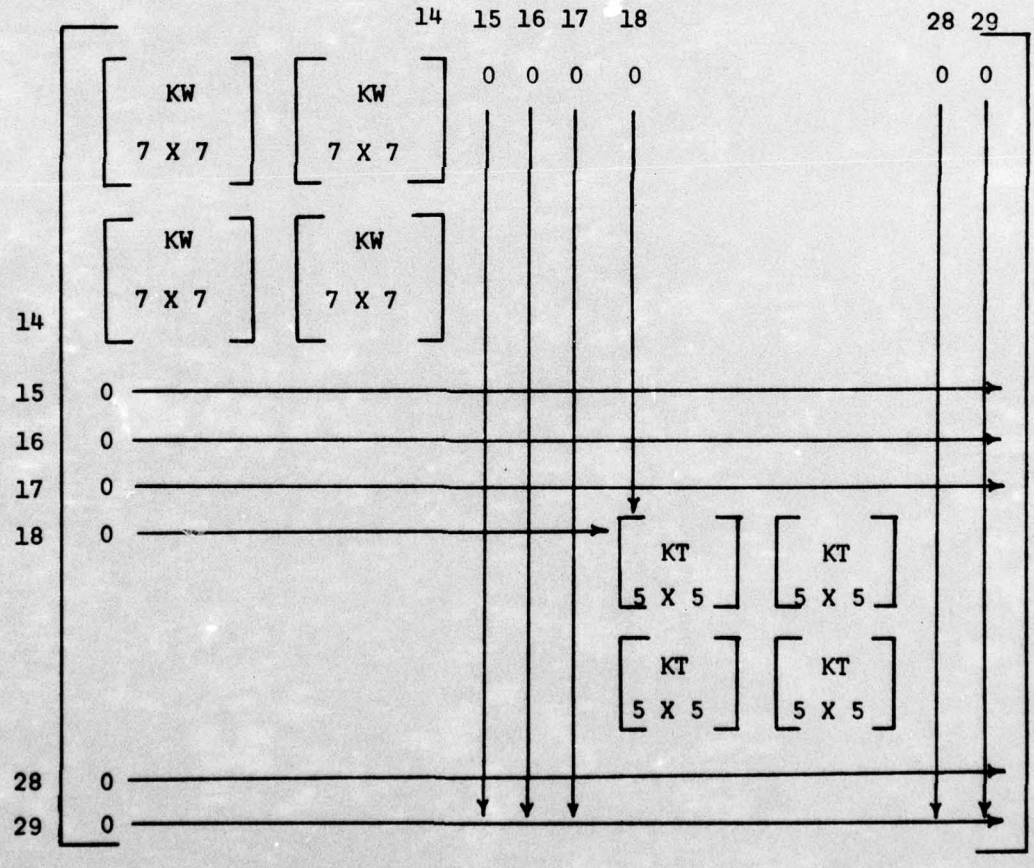

C. Assemble Overall Flexibility

1. Assemble wing sector of matrix (S(I,J),I,J = 1,17)

   a. S(I,J) = K(I,J)+T(I,J)*D(I)*D(J)+R*B(I)*B(J)+F*BF(I)
   *BF(J)+P*Y(I)*Y(J)

      1. D(I) = Distance of point I from spar center line
      2. B(I) = distance of point I from roll spring axis (roll spring moment arm)
      3. BF(I) = distance of point I from roll spring axis
      4. Y(I) = distance of point I from pitch spring axis (pitch spring moment arm)

2. Assemble tail section of matrix (S(I,J),I,J=18,27)

   a. S(I,J)+K(I,J)+T(I,J)*D(I,J)*D(I,J).

3. Add tail pitch flexibility (S(I,J),I,J=18,28)

   S(I,J) = TPD(I)*TPD(J)*TPF

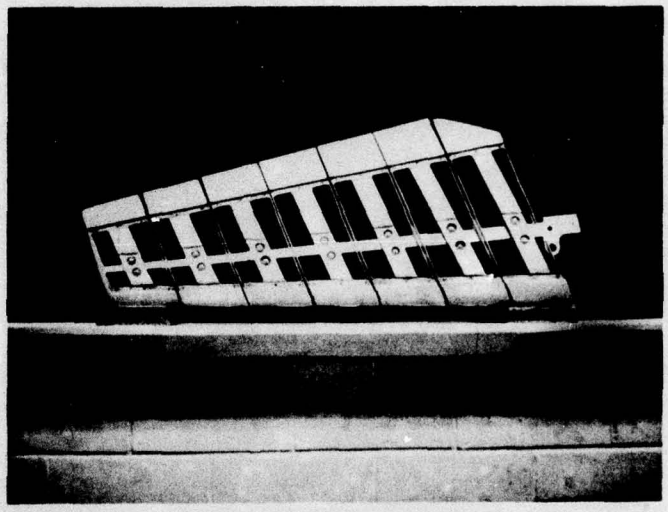

Figure C.1. Detail of Wing Construction

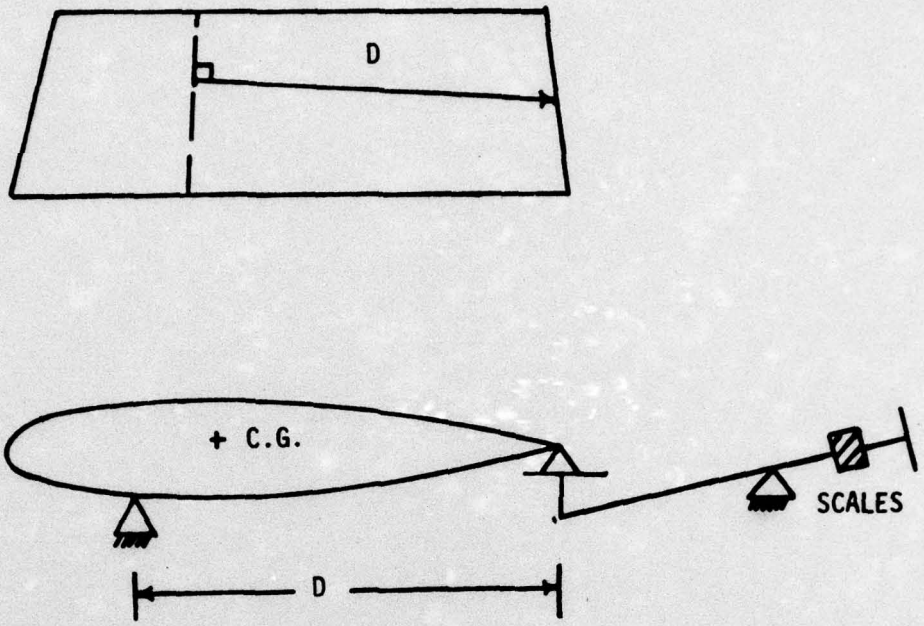

Figure C.2. Schematic of Static Unbalance Measurements

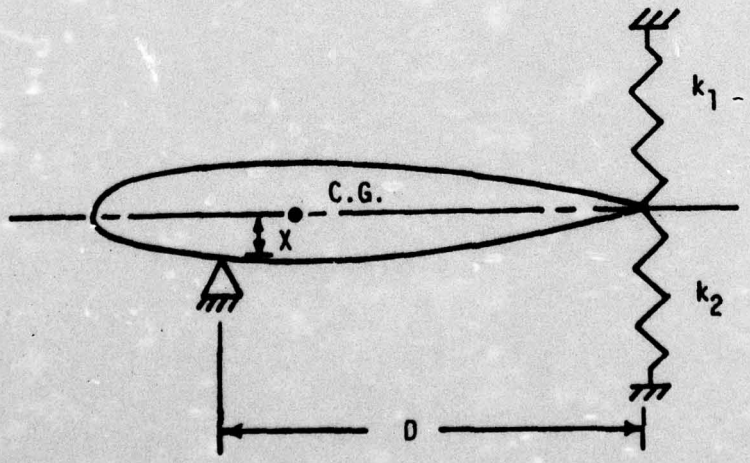

Figure C.3. Schematic of Inertia Measurements

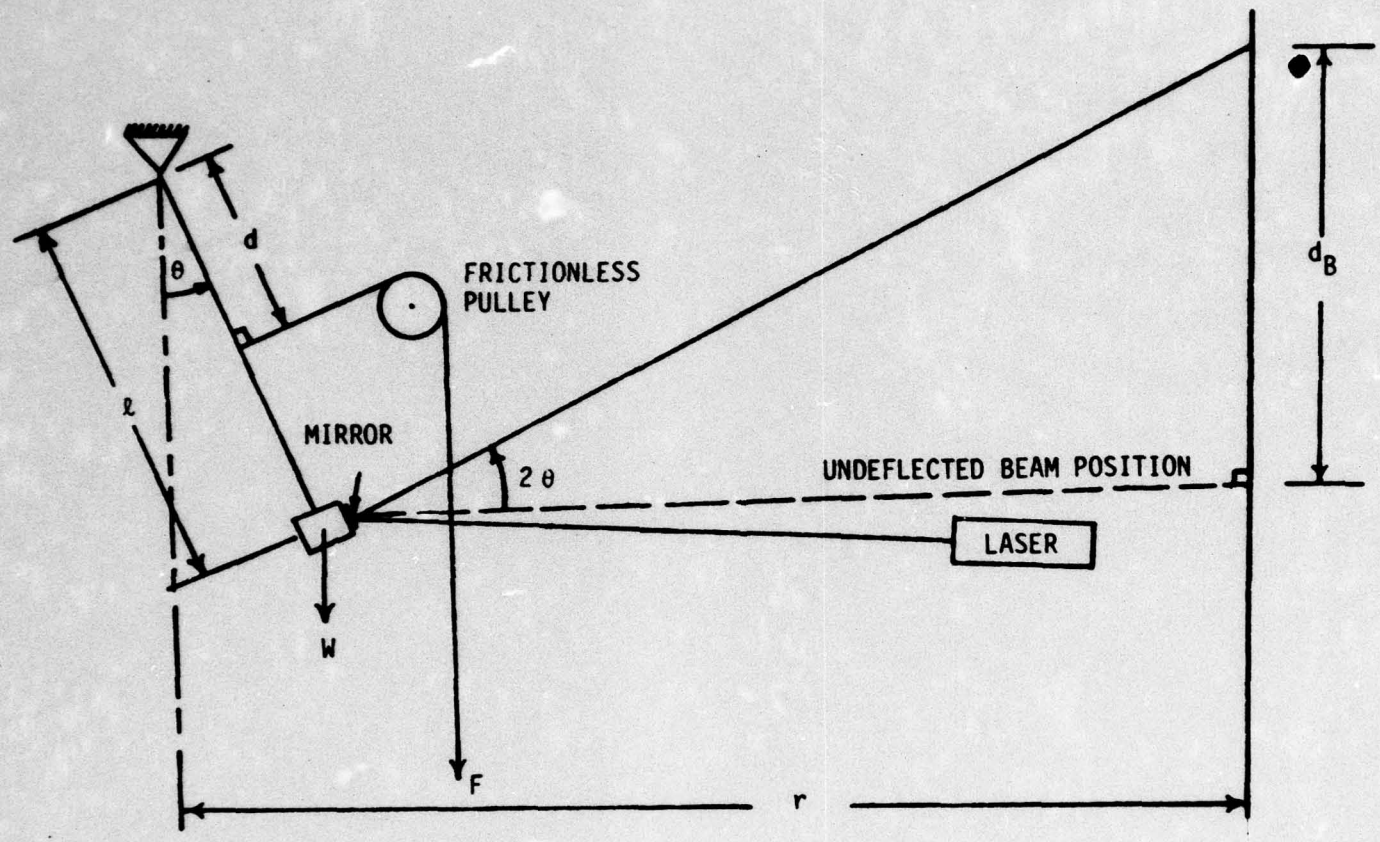

Figure C.4.Schematic of Fuselage Roll Inertia Measurement

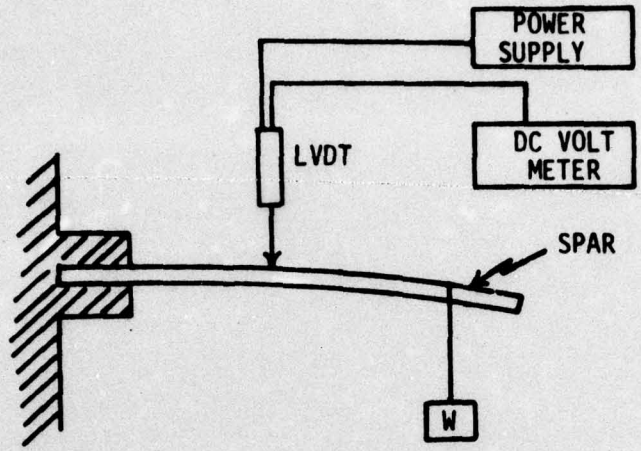

Figure C.5. Schematic of Spar Bending Flexibility Measurement

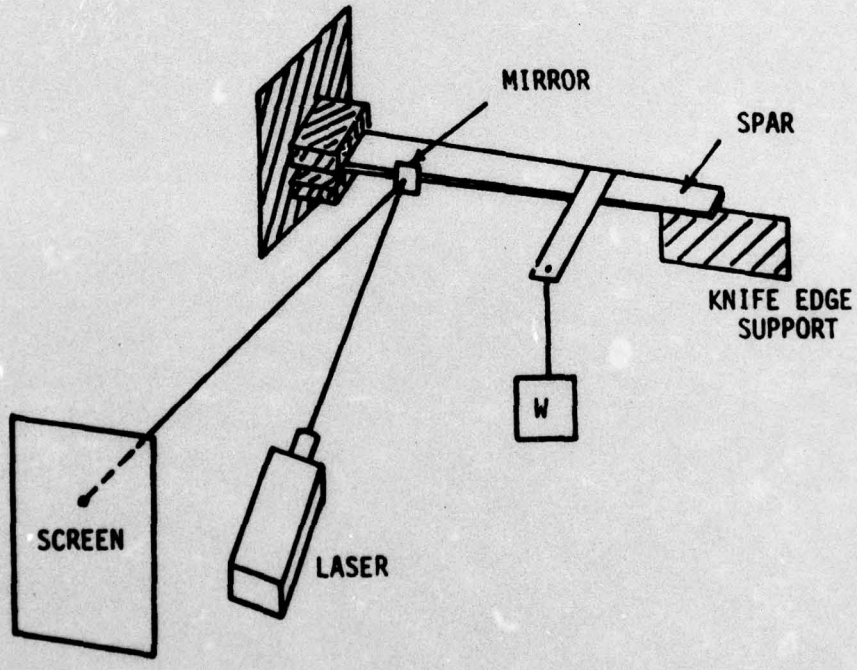

Figure C.6. Schematic of Spar Torsional Flexibility Measurement

Appendix D

Calculation of Mode Shapes of a Free-Free Structure

The structural dynamic model of the U-T wing tail wind tunnel flutter model is a lumped parameter model using discrete influence coefficients. The system is considered free-free with a rigid body roll degree of freedom. (The rigid body roll degree of freedom actually acts against a weak gravity spring but for our purposes we will call the system semidefinite). In order that the flexibility influence coefficients be defined we want to express the absolute motion in terms relative to the rigid body motion. The system can be transformed to a positive definite system by using a constraint matrix[9]:

$$[C] = [I] - \frac{1}{I_c} \{x\} \{x\}^T [M] \qquad (D.1)$$

where

$[I]$ = the identity matrix

I_c = mass moment of inertia of the whole structure about the roll axis

$\{x\}$ = the unit rigid body motion vector

$[M]$ = lumped mass matrix.

The constrained mass matrix may now be calculated by

$$[M'] = [C]^T [M] [C] \qquad (D.2)$$

and used in the eigenvalue equation

$$[M'] [h_r] = [K] [h_r] [\omega^2] \tag{D.3}$$

where

$[h_r]$ is the matrix of eigenvectors of relative motion.

Next, an absolute motion eigenvector may be calculated by transforming back:

$$\{h_A\}_j = [C] \{h_r\}_j \tag{D.4}$$

It is shown in reference 8 that

$$\{h_A\}_j = \{h_r\}_j + \{x\} \{h_p\} \tag{D.5}$$

where

$\{h_p\}$ = the vector of the rigid body reference point motion (or the plug mass in the terms of reference 8). (In our case $\{h_p\}$ is a scalar representing a rigid body roll angle.)

Comparing (D.4), (D.5) and (D.1),

$$\{h_p\} = -\frac{1}{I_c} \{x\}^T [M] \{h_r\}_j \quad .$$

The rigid body mode $\{h_A\}_{rigid}$ may be calculated by:

$$\{h_A\}_{rigid} = \{x\} \{h_p\} \tag{D.6}$$

since $\{h_p\}$ is the amount of rigid body motion and $\{x\}$ is the vector of displacements of structural points for a unit rigid body motion.

Appendix E

Visicorder Traces

Visicorder Traces Legend

Trace A: Tail Bending

Trace B: Wing Accelerometer

Trace C: Tail Accelerometer

Trace D: Wing Bending

Trace E: Tail Pitch

Trace F: Wing Torsion (when present)

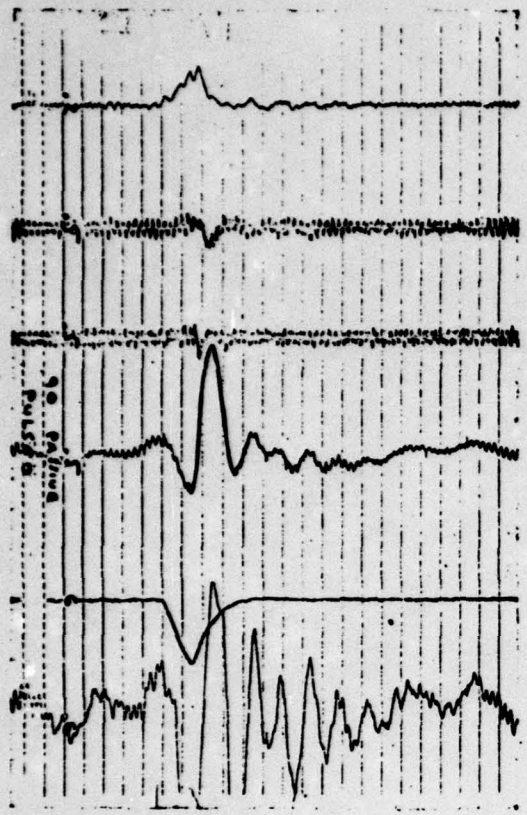

90 mph; Pulsed Excitation;
Controls Inactive;
60° Wing Sweep.

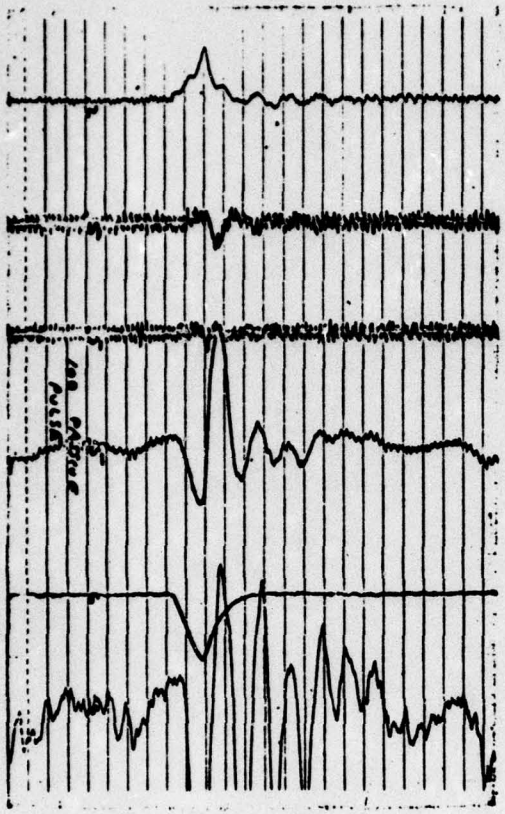

100 mph; Pulsed Excitation;
Controls Inactive;
60° Wing Sweep.

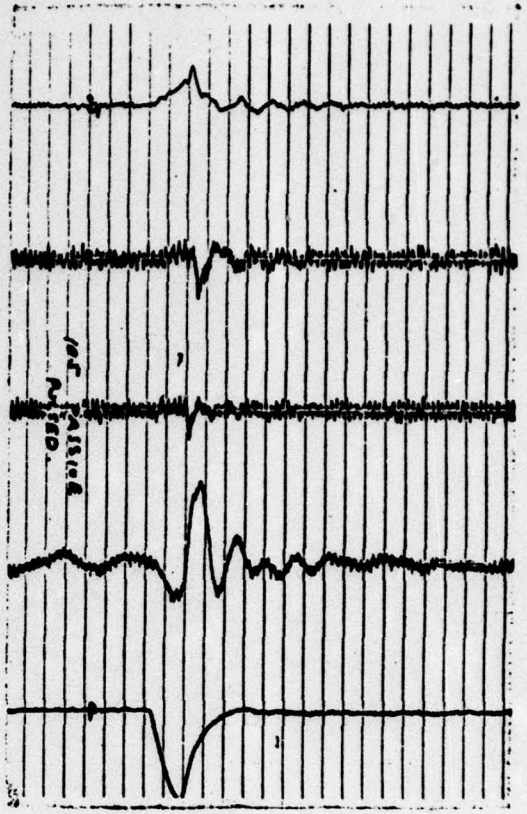

105 mph; Pulsed Excitation;
Controls Inactive;
60° Wing Sweep.

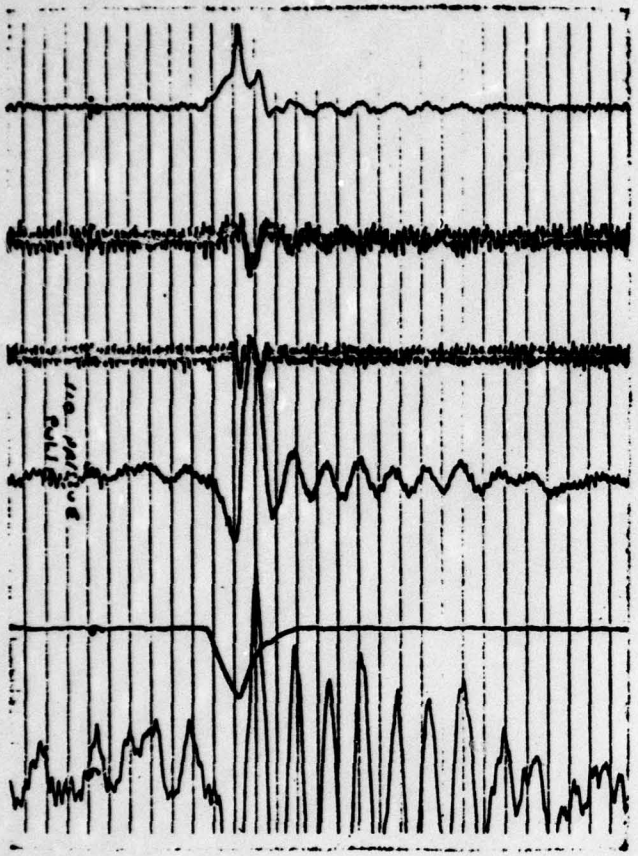

110 mph; Pulsed Excitation;
Controls Inactive;
60° Wing Sweep.

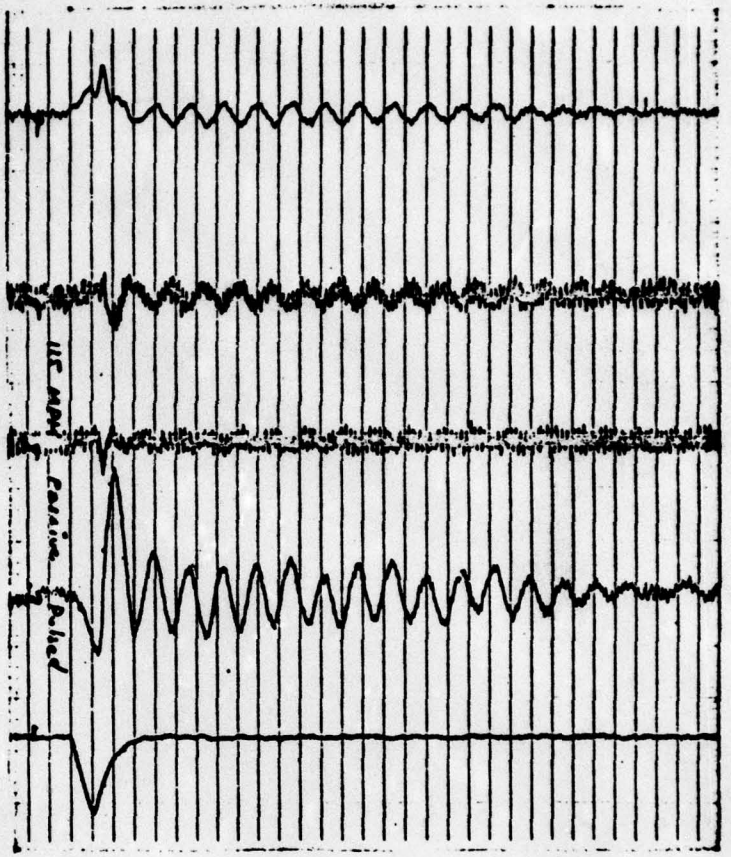

115 mph; Pulsed Excitation;
Controls Inactive;
60° Wing Sweep.

AD-A039 216 TEXAS UNIV AT AUSTIN DEPT OF AEROSPACE ENGINEERING AN--ETC F/G 20/4
WIND TUNNEL EXPERIMENTS ON AN ACTIVELY CONTROLLED, VARIABLE GEO--ETC(U)
MAR 77 J LONG, R STEARMAN F44620-76-C-0072

UNCLASSIFIED AFOSR-TR-77-0638 NL

2 OF 2
AD A039216

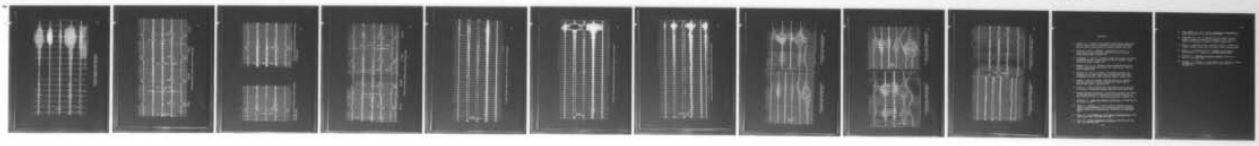

END

DATE FILMED
5-77

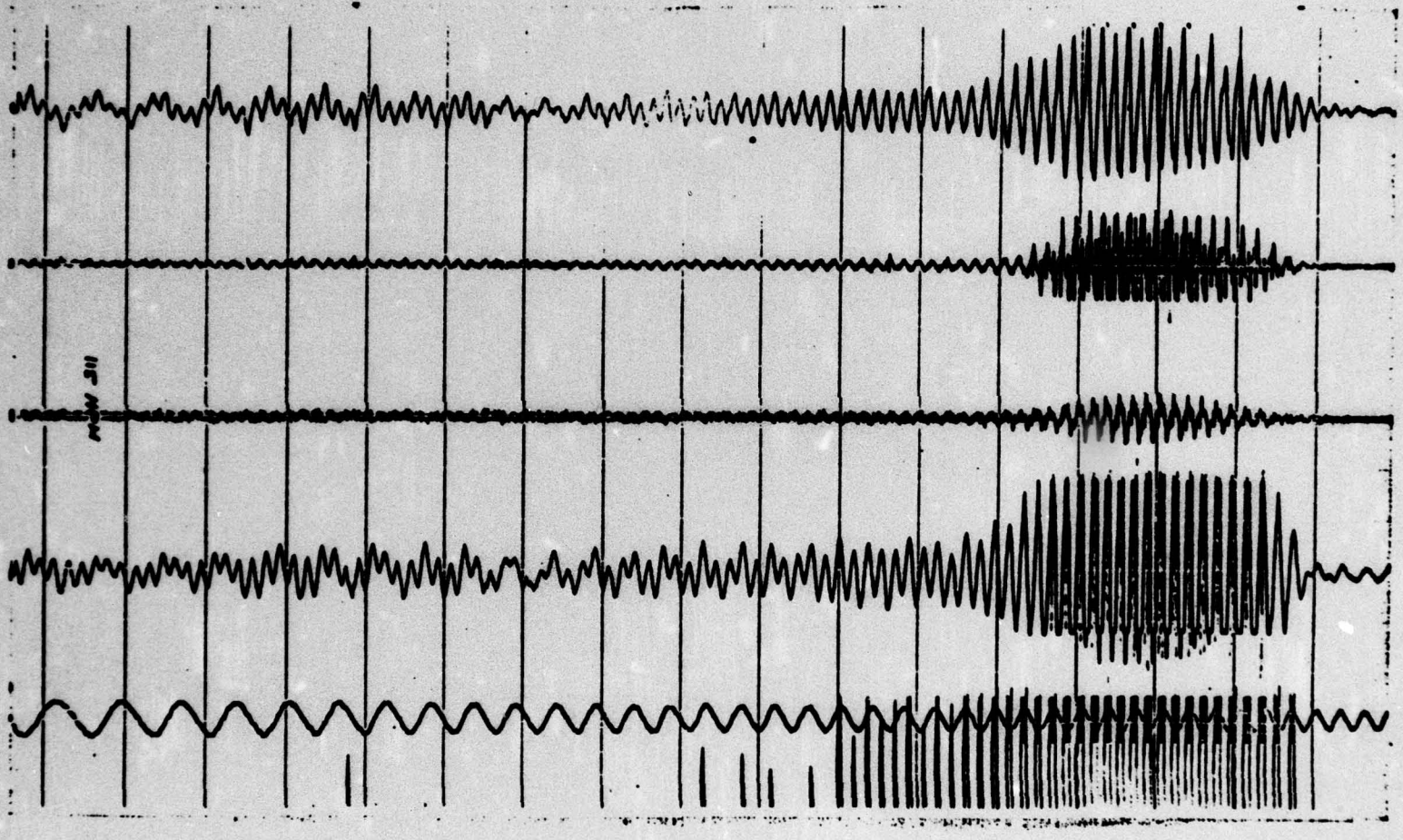

115 mph; Frequency Sweep Excitation;
Controls Inactive; 60° Wing Sweep.

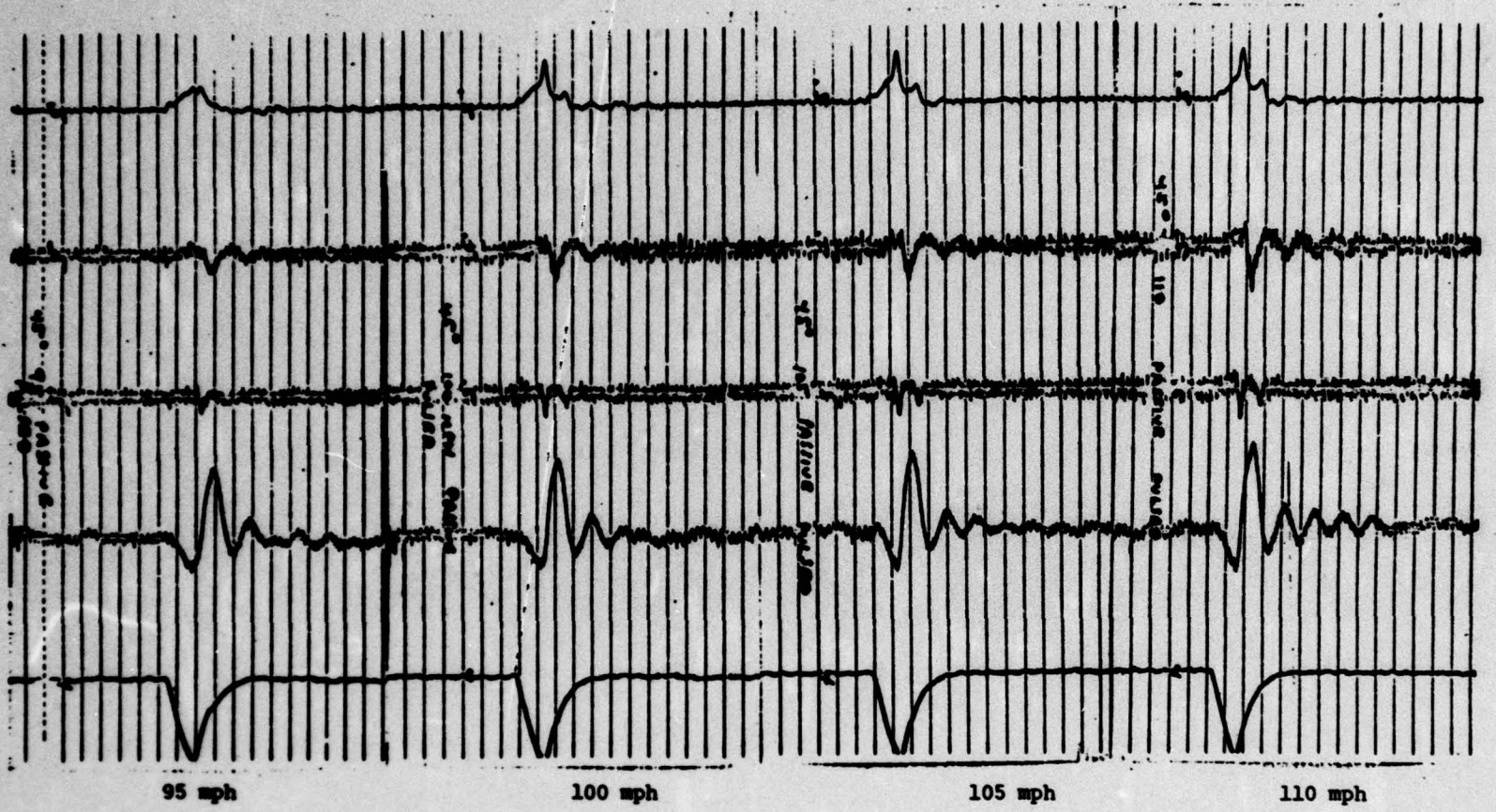

Pulsed Excitation; Controls Inactive; 45° Wing Sweep

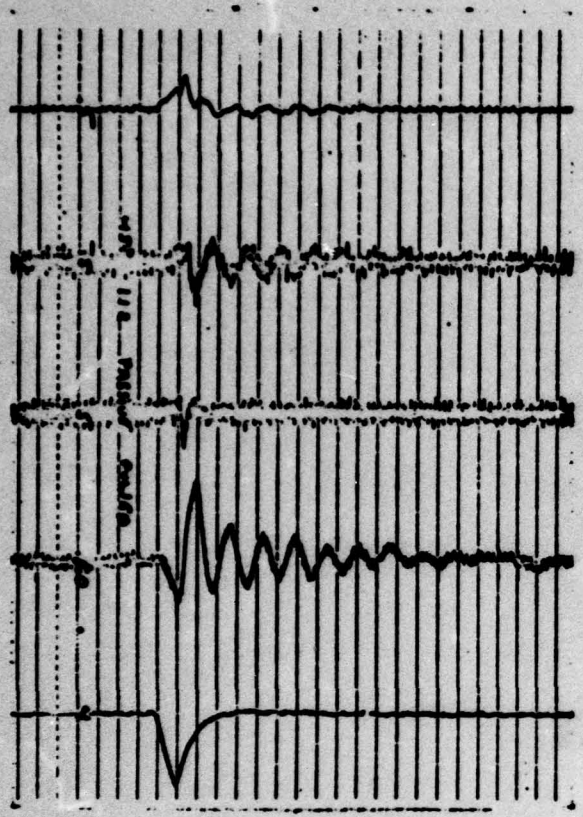

112 mph; Pulsed Excitation; Controls Inactive;
45° Wing Sweep

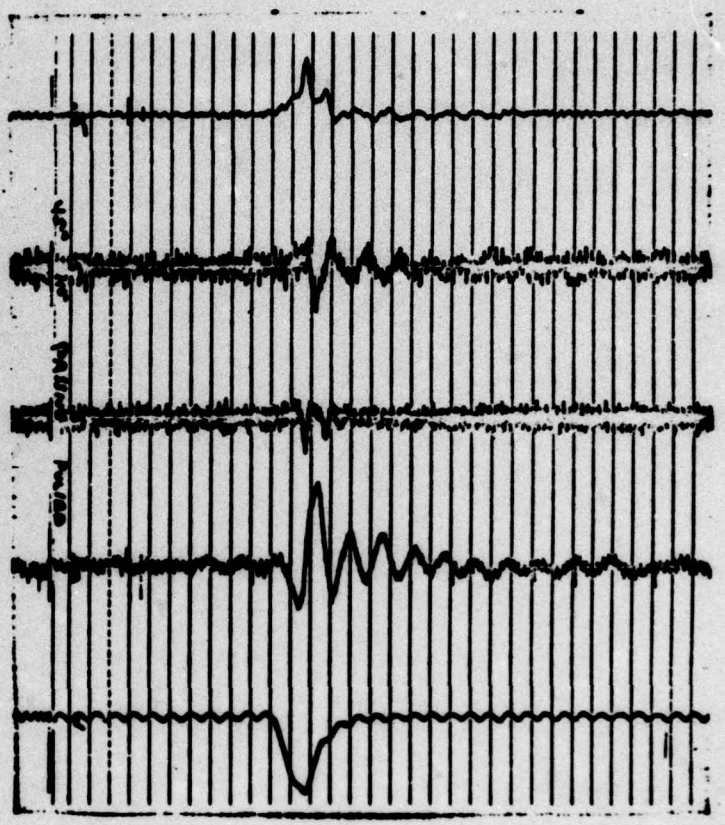

115 mph; Pulsed Excitation; Controls Inactive;
45° Wing Sweep

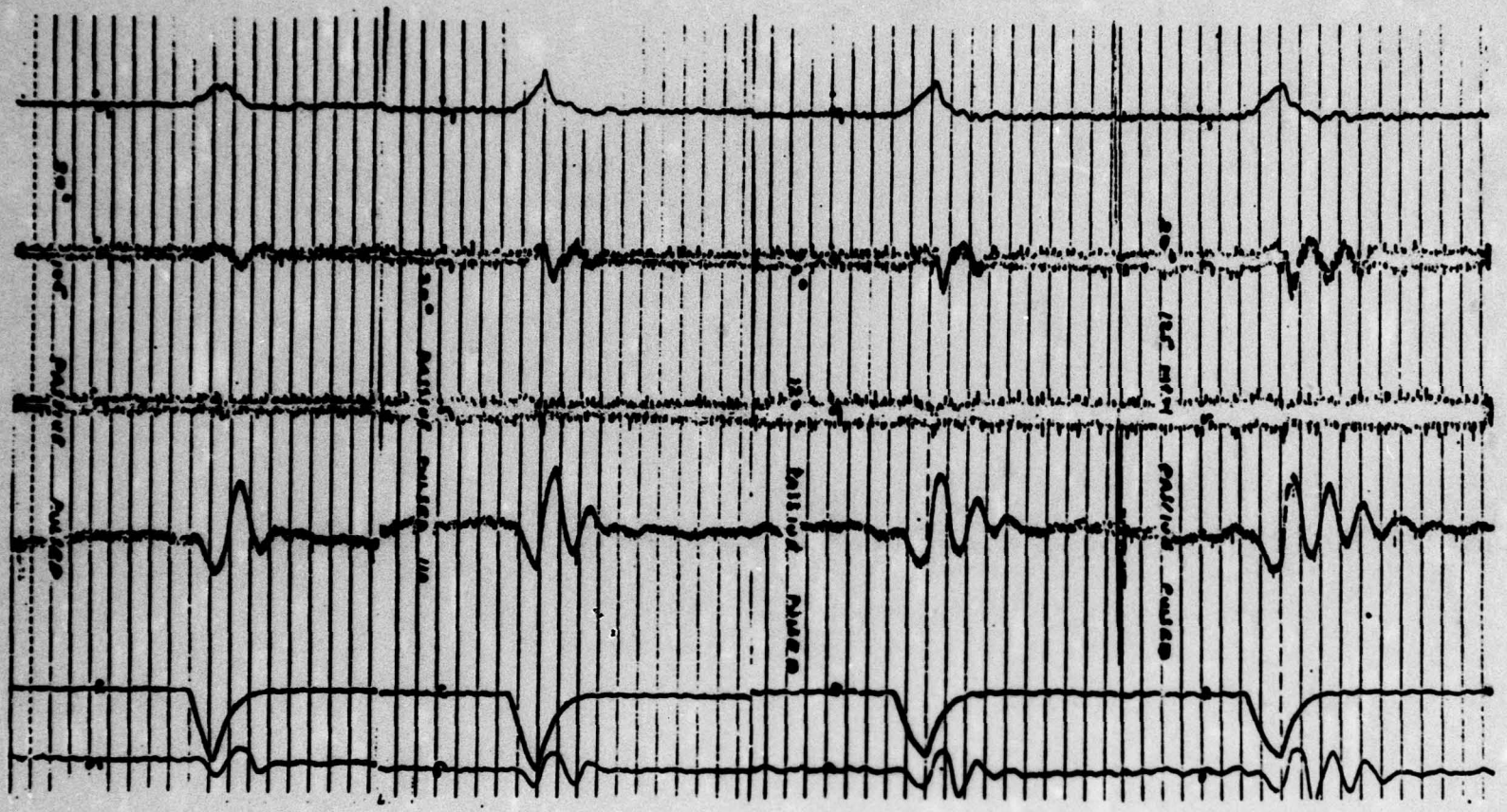

105 mph 110 mph 120 mph 125 mph

Pulsed Excitation; Controls Inactive; 30° Wing Sweep

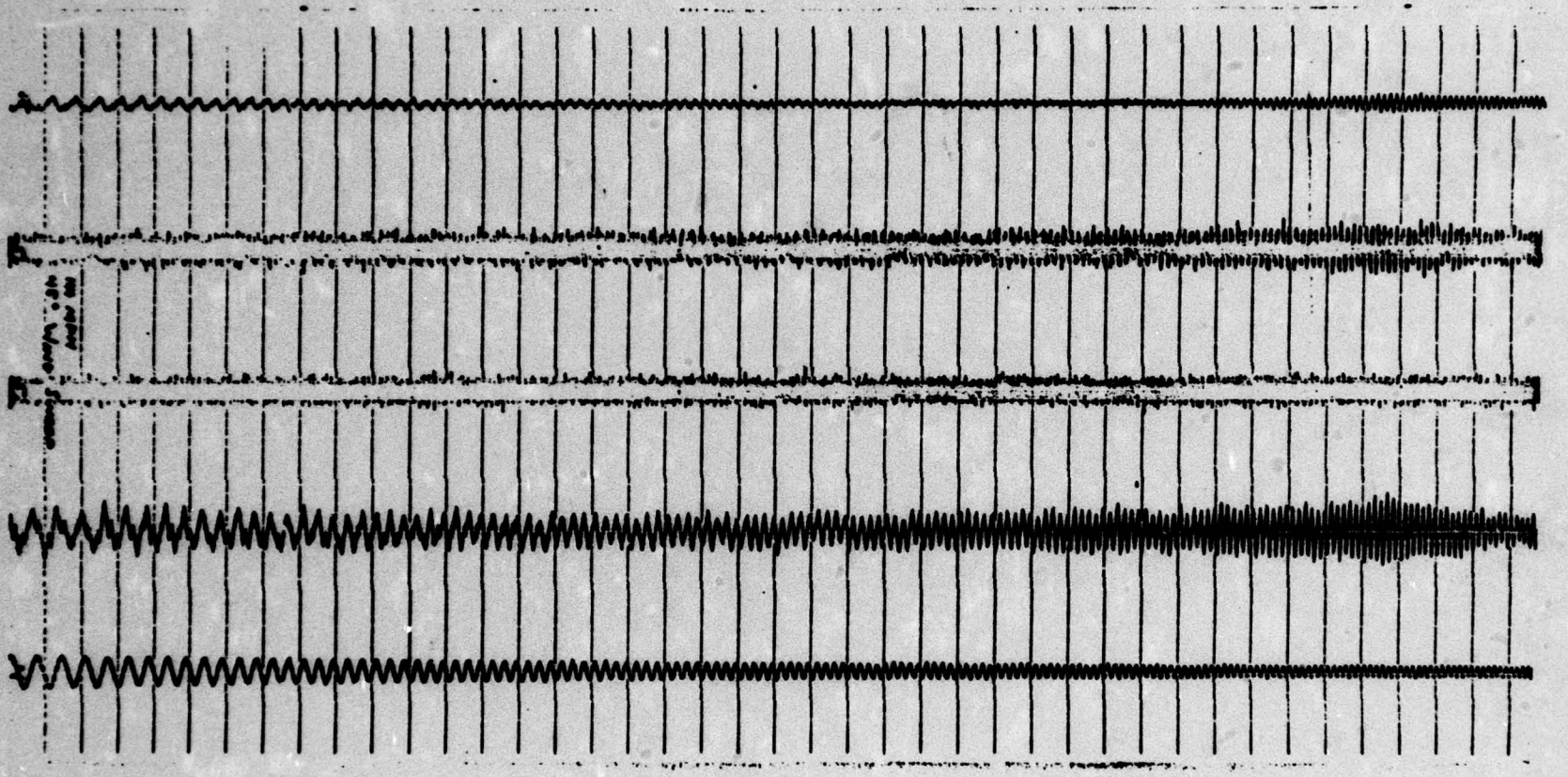

114 mph; Frequency Sweep Excitation; Controls Inactive; 45° Wing Sweep

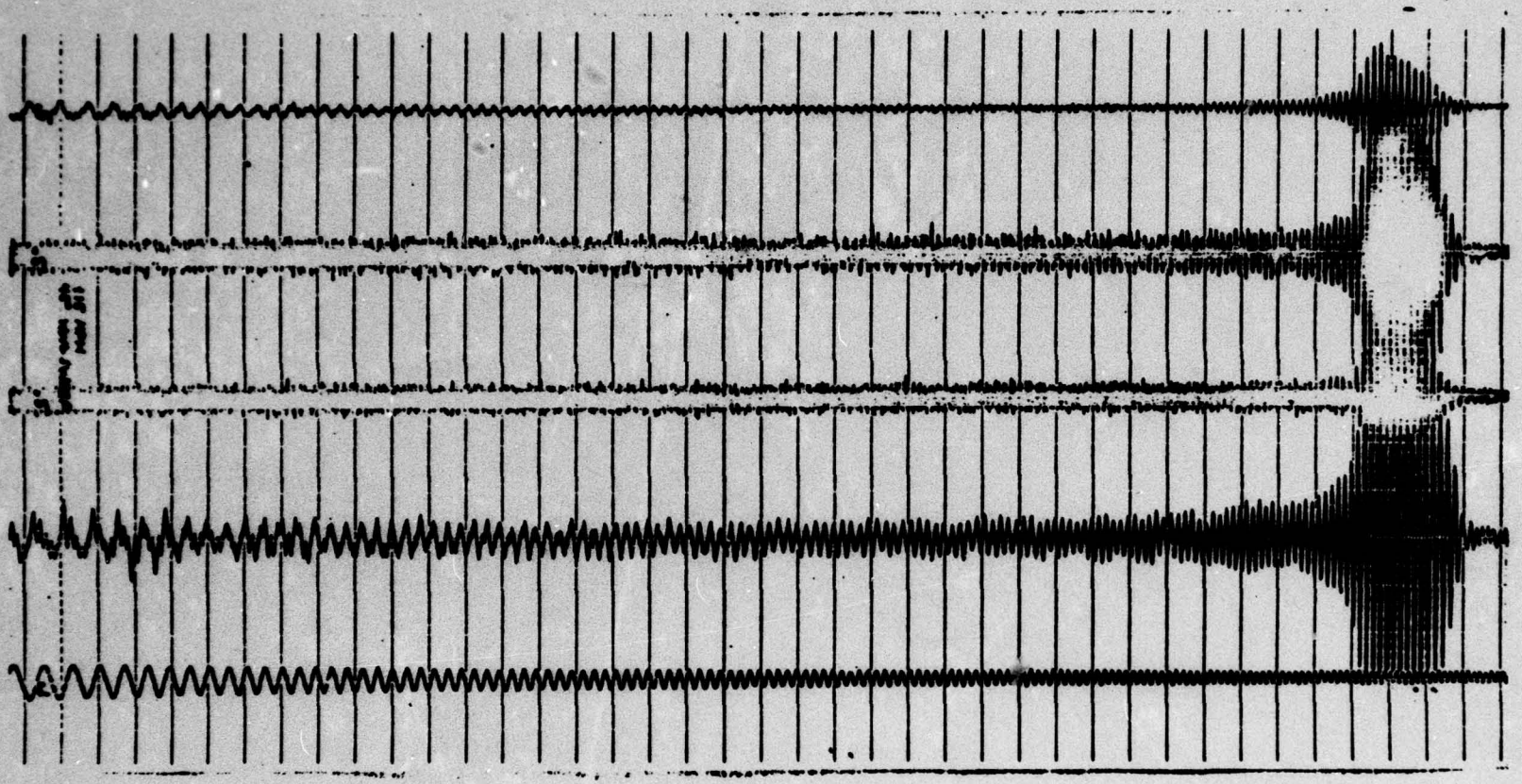

115 mph; Frequency Sweep Excitation; Controls Inactive; 45° Wing Sweep

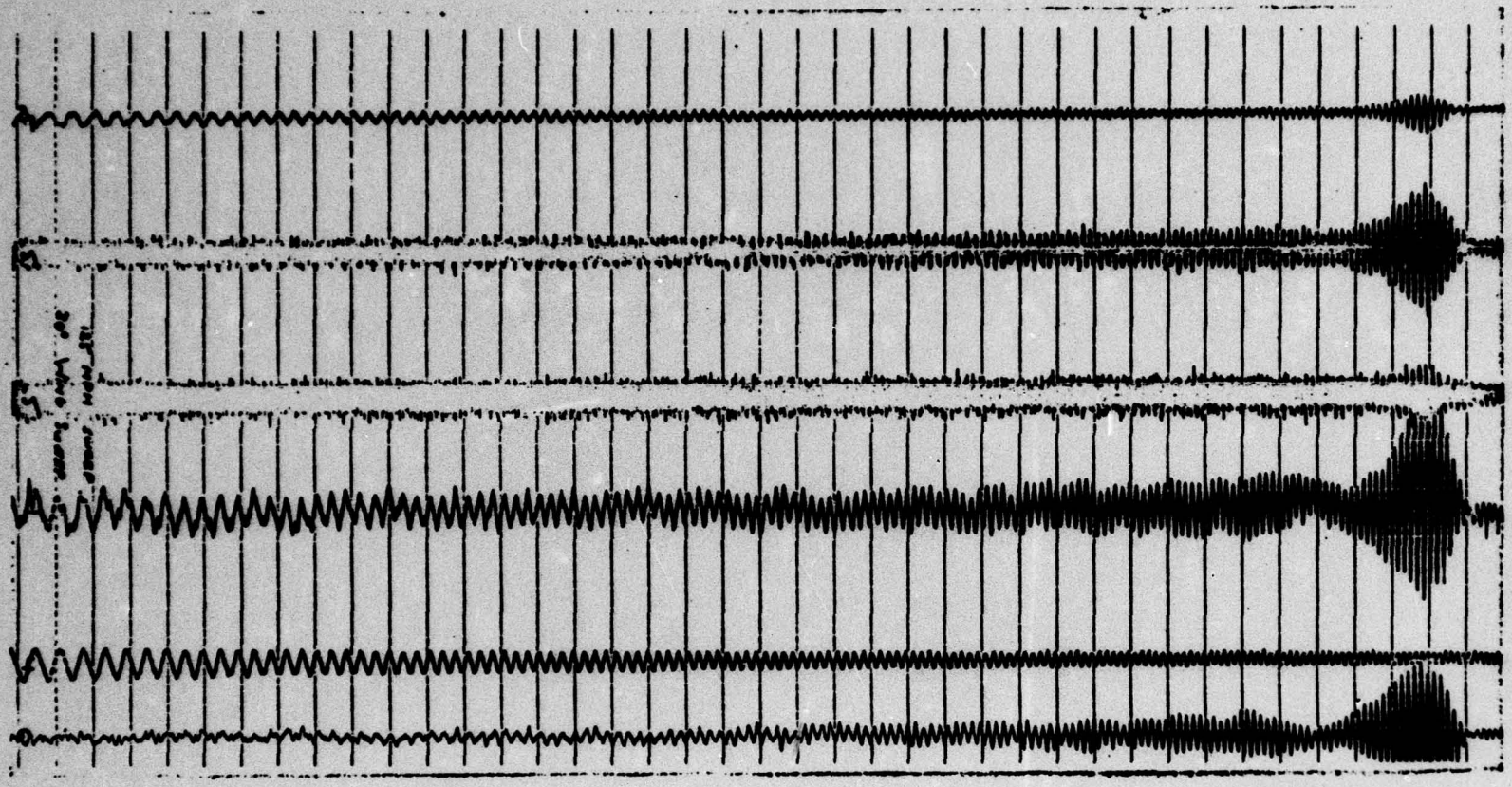

125 mph; Frequency Sweep Excitation; Controls Inactive; 30° Wing Sweep

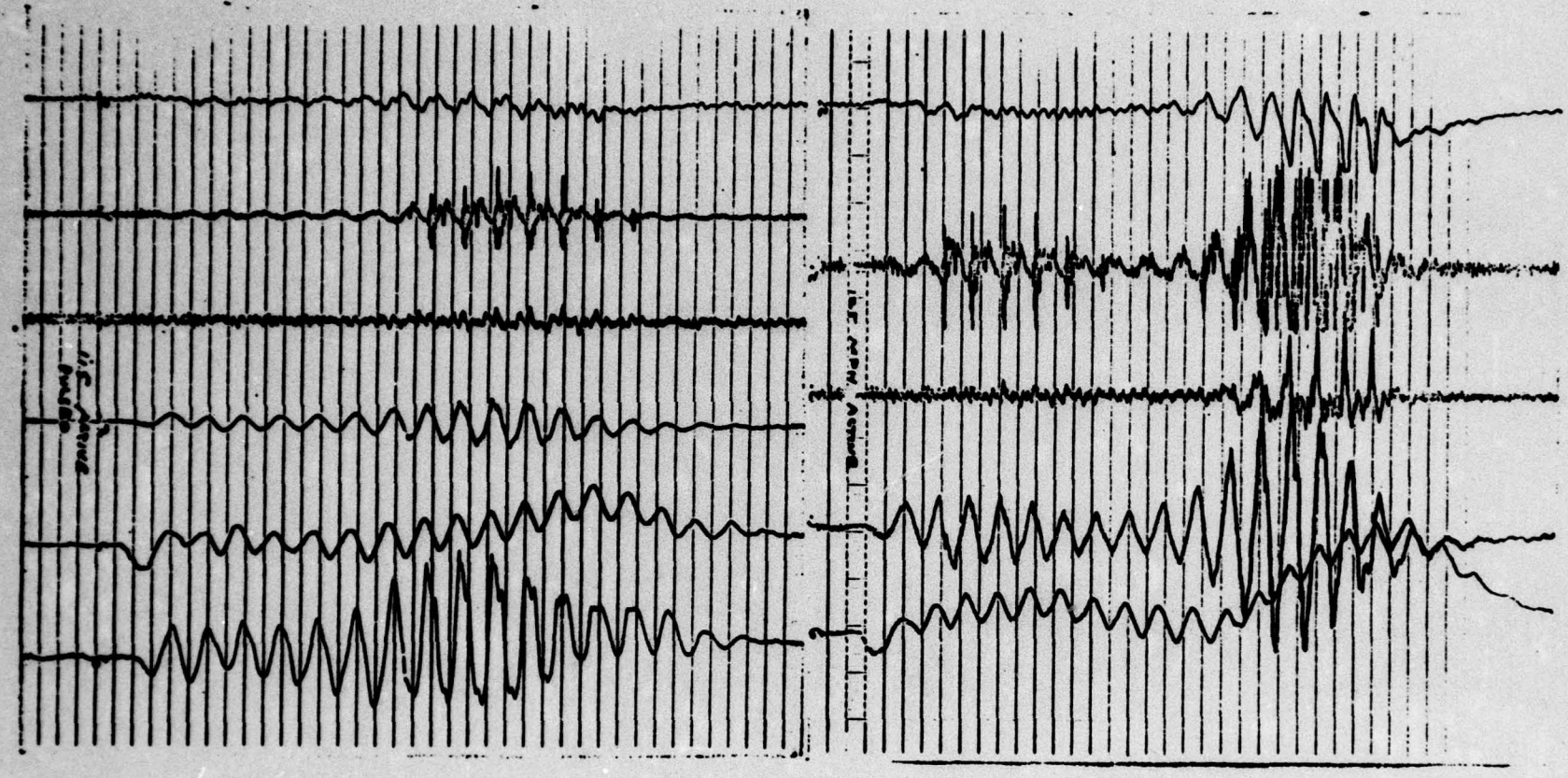

115 miles per hour; Pulsed Excitation;
Controls Active; 60° Wing Sweep.

125 miles per hour; Pulsed Excitation;
Controls Active: 60° Wing Sweep.

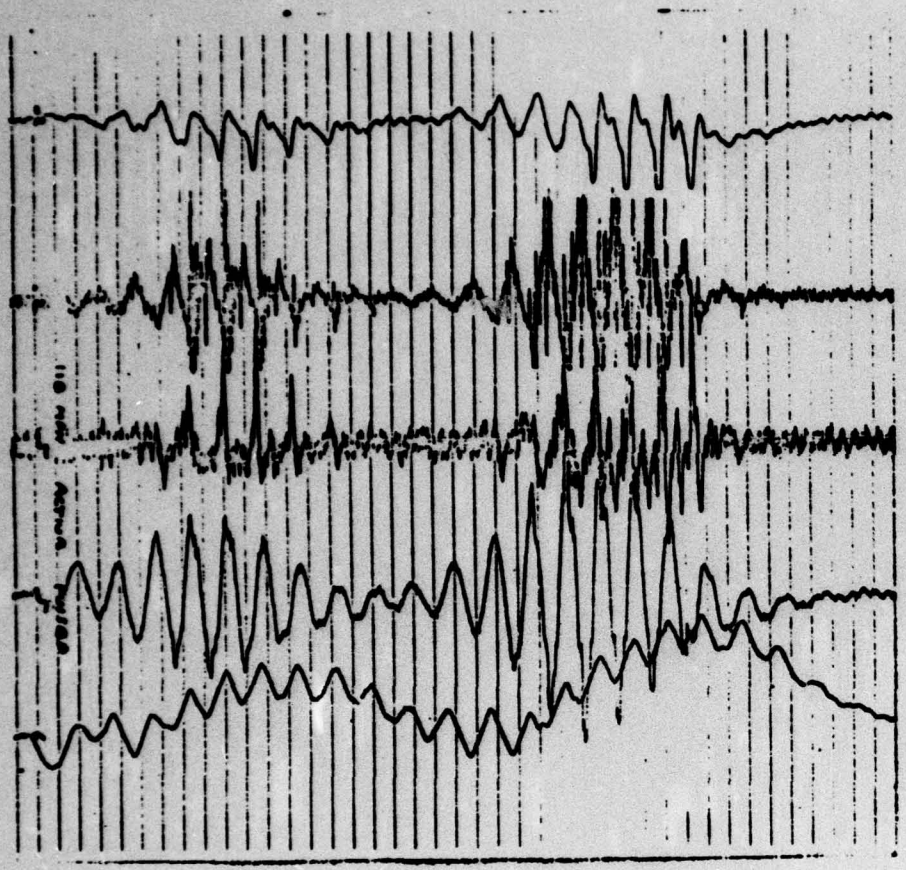

118 miles per hour; Pulsed Excitation;
Controls Active; 60° Wing Sweep.

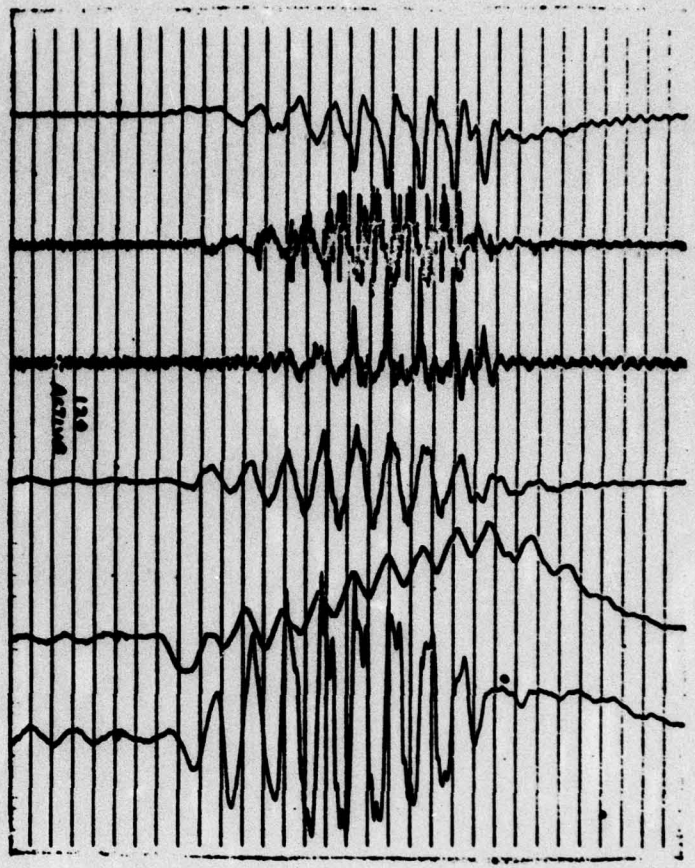

120 miles per hour; Pulsed Excitation;
Controls Active; 60° Wing Sweep.

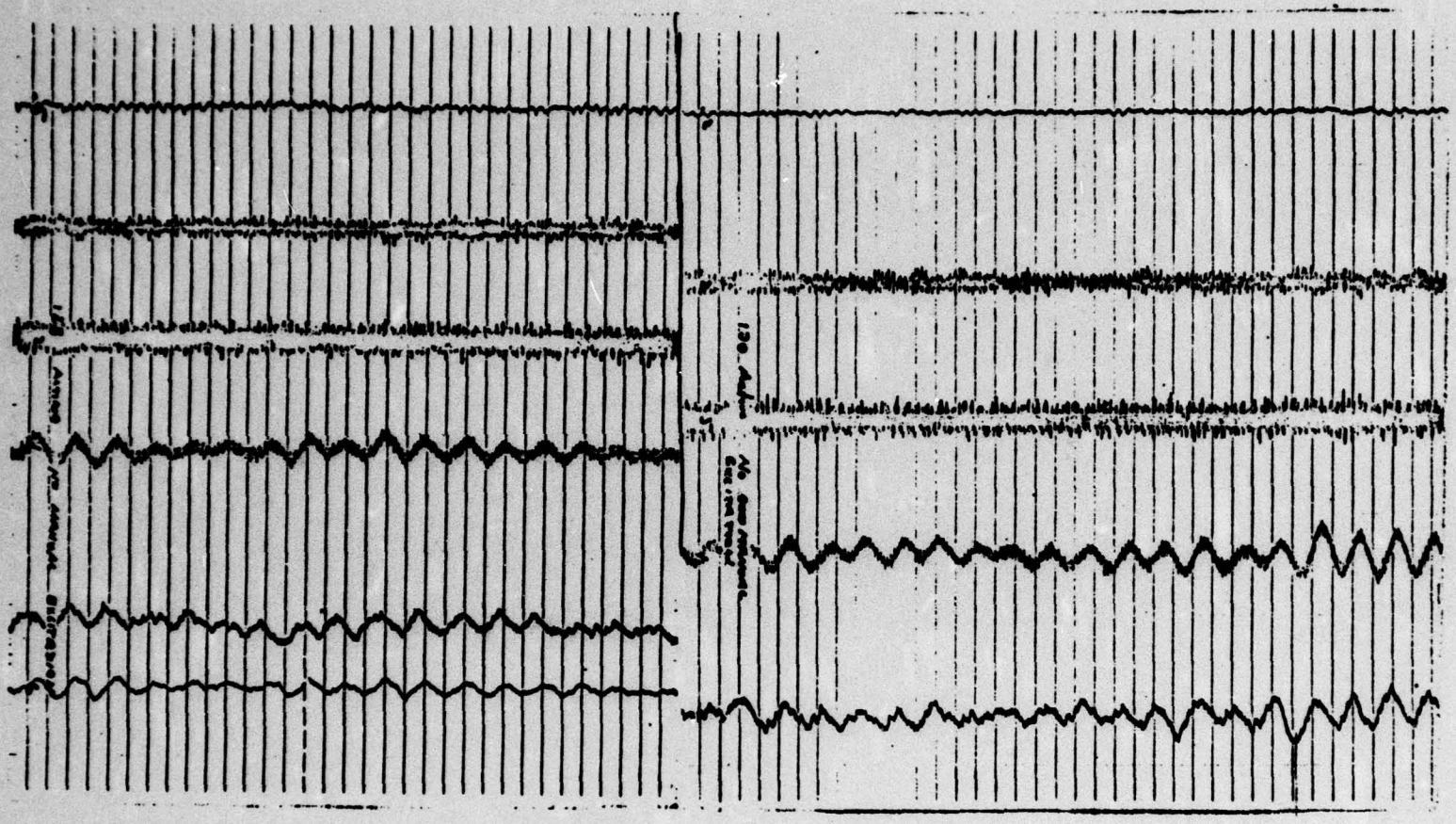

128 miles per hour; No Manual Excitation;
Controls Active; 60° Wing Sweep.

130 miles per hour; No Manual Excitation;
Controls Active; 60° Wing Sweep.

References

1. Griffin, K.E., "Flutter Characteristics and Feedback Suppression Results for Two Modes of Interference Lifting Surface Flutter," Master's Thesis, The University of Texas at Austin, May 1972.

2. Cwach, E.E. and R.O. Stearman, "Suppression of Flutter on Interfering Lifting Surfaces by the Use of Active Controls," AFOSR Interim Report, January 1974.

3. Pinnamaneni, R. and R.O. Stearman, "Design and Analysis of Flutter Suppression Systems through the Use of Active Controls," AFOSR Scientific Report, January 1975.

4. Mykytow, W.J., et al., "Subsonic Flutter Characteristics of a Variable Sweep Wing and Horizontal Tail Combination," AFFDL-TR-69-59, November 1970.

5. Bolding, R.M. and R.O. Stearman, "The Design, Analysis, and Testing of a Low Budget Wind Tunnel Flutter Model with Active Aerodynamic Controls," AFOSR Scientific Report, January 1976.

6. Lehman, L. and R.O. Stearman, "Flutter Studies of a Subsonic, Actively Controlled, Variable Geometry Wind Tunnel Model," AFOSR Interim Report, September 1976.

7. Nissim, E., "Flutter Suppression Using Active Controls Based on the Concept of Aerodynamic Energy," NASA TN D-6199, March 1970.

8. Grumman Aerospace Corporation, "An Automated Procedure for Flutter and Strength Analysis and Optimization of Aerospace Vehicles," AFFDL-TR-75-137, Vol. I: Theory and Application, December 1975.

9. Meirovitch, L., Analytical Methods in Vibrations, The Macmillan Co., New York, NY, 1967.

10. Albano, E., Perkinson, R., and W.P. Rodden, "Subsonic Lifting-Surface Theory AErodynamics and Flutter Analysis of Interfering Wing/Horizontal-Tail Configurations," AFFDL-TR-70-59, September 1970.

11. Fung, Y.C., An Introduction to the Theory of Aeroelasticity, Dover Publications, Inc., New York, NY, 1969.

12. Tong, K.N., Theory of Mechanical Vibration, John Wiley and Sons, Inc., New York, NY, 1960.

13. Bisplinghoff, R.L. and H. Ashley, Principles of Aeroelasticity, Dover Publications, Inc., New York, NY, 1975.

14. Frederick, W.A., Jr., "A Composite Flutter Analysis Fortran Computer Program for Subsonic and Supersonic Flow," Master's Thesis, The University of Texas at Austin, August 1970.

15. Waner, P., "Analysis of Gust Alleviation Devices," ERR-FW-1018, General Dynamics Corporation, Fort Worth, Texas, December 1969.

16. Hurty, W.C. and Rubenstein, M.F., Dynamics of Structures, Prentice-Hall Inc., Inglewood Cliffs, New Jersey, 1964.

17. Merovitch, L., Methods of Analytical Dynamics, McGraw-Hill Book Co., New York, 1970.

18. Giesing, J.P., Kalman, T.P., and Rodden, W.P., "Subsonic Unsteady Aerodynamics for General Configurations," AFFDL-TR-71-5, November 1971.

UNCLASSIFIED

SECURITY CLASSIFICATION OF THIS PAGE (When Data Entered)

REPORT DOCUMENTATION PAGE	READ INSTRUCTIONS BEFORE COMPLETING FORM
1. REPORT NUMBER: AFOSR-TR-77-0698	2. GOVT ACCESSION NO.
3. RECIPIENT'S CATALOG NUMBER	
4. TITLE (and Subtitle): WIND TUNNEL EXPERIMENTS ON AN ACITVELY CONTROLLED, VARIABLE GEOMETRY FLUTTER MODEL- VOL II	5. TYPE OF REPORT & PERIOD COVERED: FINAL rept. 1 Feb 76 - 31 Jan 77
	6. PERFORMING ORG. REPORT NUMBER
7. AUTHOR(s): Jeff Long, Ronald Stearman — Volume II.	8. CONTRACT OR GRANT NUMBER(s): F44620-76-C-0072
9. PERFORMING ORGANIZATION NAME AND ADDRESS: The University of Texas at Austin, Dept. of Aerospace Engr. and Engr. Mechanics, Austin, Texas 78712	10. PROGRAM ELEMENT, PROJECT, TASK AREA & WORK UNIT NUMBERS: 9782.04, 2307/B1
11. CONTROLLING OFFICE NAME AND ADDRESS: Air Force Office of Scientific Research/NA, Building 410, Bolling Air Force Base, D.C. 20332	12. REPORT DATE: March 1977
	13. NUMBER OF PAGES: 105
14. MONITORING AGENCY NAME & ADDRESS(if different from Controlling Office): 04, B1	15. SECURITY CLASS. (of this report): UNCLASSIFIED
	15a. DECLASSIFICATION/DOWNGRADING SCHEDULE

16. DISTRIBUTION STATEMENT (of this Report)

APPROVED FOR PUBLIC RELEASE; DISTRIBUTION UNLIMITED. 108p.

17. DISTRIBUTION STATEMENT (of the abstract entered in Block 20, if different from Report)

18. SUPPLEMENTARY NOTES

19. KEY WORDS (Continue on reverse side if necessary and identify by block number)

Flutter Suppression
Active Control
Wind Tunnel Flutter Model

20. ABSTRACT (Continue on reverse side if necessary and identify by block number)

A reduction in flutter margin can occur for variable geometry aircraft when the wing of the aircraft is swept into the vicinity of the tail. Experiments on an aeroelastic wind tunnel model with active aerodynamic controls demonstrated that the flutter margins of these configurations can be increased through techniques other than the standard structural modifications. Improved margins were attained experimentally by employing rapidly responding aerodynamic controls activated by an "optimal" feedback.

DD FORM 1 JAN 73 1473 EDITION OF 1 NOV 65 IS OBSOLETE

UNCLASSIFIED

SECURITY CLASSIFICATION OF THIS PAGE (When Data Entered)

402465